DEVELOPMENT OF A LOW-COST CAVITY RING-DOWN SPECTROMETER

A thesis presented to the faculty of the Graduate School of Western Carolina University in partial fulfillment of the requirements for the degree of Masters of Science in Chemistry.

By

Charles Wise

Advisor: Dr. Al Fischer
Assistant Professor of Chemistry
Department of Chemistry & Physics

Committee Members: Dr. Scott Huffman, Chemistry & Physics
Dr. David Butcher, Chemistry & Physics

December 2023

ACKNOWLEDGEMENTS

Western Carolina University

Dr. Al Fischer

Dr. Scott Huffman

Dr. David Butcher

Wesley W. Bintz

Matt Burleson

Dr. Geoffrey Smith

TABLE OF CONTENTS

LIST OF TABLES

LIST OF FIGURES

ABSTRACT

DEVELOPMENT OF A LOW-COST CAVITY RING-DOWN SPECTROMETER

Charles Wise, M.S., Chemistry

Western Carolina University (December 2023)

Advisor: Dr. Al Fischer

Airborne analytes are often hard to measure due to their small concentrations (ppm-ppb), especially those in our atmosphere. Airborne analytes such as ozone, nitrogen dioxide, and black carbon are commonly studied for climate modeling and their pollution contribution. Common commercial analytical instruments are usually not equipped to handle those detection limits, and if they are, they come at a higher cost and lack portability. Cavity ring-down spectroscopy (CRDS) resolves many of these attributes common commercial instruments cannot produce and is commonly employed in atmospheric research. Low-cost instruments are also becoming increasingly popular in higher levels of research because of their price and ability to be highly specific to a research group's needs. The goal of this project is to bridge both concepts by building two low-cost CRDS with commercial (kinematic system) and 3D-printed (cage system) parts and comparing their performance against themselves and a high-cost CRDS. This was accomplished by testing the drift of each design through Allan deviation calculations and validating the kinematic system results by measuring the absorption cross sections (σ) of O_3 and NO_2. The σ_{O_3-445} measurement was within 8% of literature values displayed with a $\pm$14% uncertainty, while σ_{NO_2-445} was within 7% of displayed literature values with a $\pm$11% uncertainty. Both designs show promise, but the cage system has better stability and will be further developed in the future.

CHAPTER 1: INTRODUCTION

Background

Motivation

Airborne analytes can be challenging to measure at trace levels.[1] Being challenging to measure is a hurdle to researchers as these analytes, such as atmospheric aerosols, are essential for building climate models.[2] Standard commercial analytical instruments such as infrared and mass spectrometers are usually not fitted to measure trace airborne analytes such as ambient aerosols or lab-generated gases.[3,4] Some can have additional components installed to measure these analytes, but that can cost many thousands of dollars on top of their already high price. Another caveat of these standard instruments is their mobility, which usually is none, so even with the outfitted additional components they still cannot be moved to locations where ambient aerosol measurements are significant for researchers. Measuring airborne analytes inside or in the field requires a different approach; a technique called cavity-enhanced spectroscopy (CES) and its popular counterpart cavity ring-down spectroscopy (CRDS) solves many of the issues mentioned above.[5]

Cavity Enhanced Spectroscopy

Cavity-enhanced spectroscopy has become increasingly popular amongst chemists for its sensitive and robust qualities.[5] CES works on a basic principle similar to lasers; it requires an optical cavity that has highly reflective (HR) mirrors ($< 99\%$) on each end of the cavity. Light is transmitted through one side of the cavity, reflecting between the mirrors once inside. The mirrors are not 100% reflective, and a small percentage of light leaks out of the cavity through the mirrors. The small percentage of light leakage and loss inside the cavity creates an exponential decay of the initially transmitted light which can be measured. The light decay time can last very long in perspective of the speed of light, and even a fraction of the light decay can be measured in the nanosecond to microsecond range.

The advantage of the cavity is longer interactions between the analyte and light. This concept

is similar to Beer-Lambert's law, where increasing the pathlength increases the light-analyte interaction, effectively increasing the sensitivity. For CES the pathlength that equates to the total distance light will travel in the cavity between the mirrors is called the effective pathlength. The effective pathlength of a CES can be roughly calculated using the following equation (Eq. 1).[6]

$$L_{eff} = \frac{L}{1 - R} \tag{1}$$

L_{eff} is the effective pathlength, L is the physical pathlength between the mirrors, and R is the reflectivity of the mirrors used in the cavity. This calculation is the simplest in determining L_{eff} and should be interpreted as the best-case scenario. Still, it provides a perspective of the sheer magnitude increase in pathlength CES could achieve. For example, if a cavity has a physical pathlength of 23 cm and the mirrors have a rated reflectivity of 99.995$\%$ or 0.99995, then the effective pathlength would be 4.6 km. By just putting two HR mirrors in a cavity the pathlength increased by a factor of $\sim$23,000.

Since airborne analytes are usually in low concentrations (ppm - ppb) and how they scatter or absorb light is an intrinsic property of the analyte, increasing the light-analyte interaction by CES is an attractive way to measure airborne analytes. There are standard well-documented techniques that use CES; cavity ring-down spectroscopy (CRDS) is a widely used technique and was used for this project.

Cavity Ring-Down Spectroscopy

Cavity ring-down spectrometers use a light source, commonly a laser, modulated into a high-finesse cavity.[6,7] Once particles are introduced into the cavity, the incident light will interact with the particles and be scattered or absorbed, causing extinction of light. This technique is a time-dependent technique, relying on the differences in exponential decay time within the cavity, often called ring-down time. The measured difference between an empty cavity ring-down time (τ_0)

and a filled cavity ring-down time (τ) is proportional to absorption inside the cavity (Eqs. 2).[6]

$$\alpha = \frac{R_l}{c}\left(\frac{1}{\tau} - \frac{1}{\tau_0}\right) \tag{2}$$

α is the extinction coefficient of the analyte in m^{-1}, R_l is the physical pathlength, c is the speed of light, τ is the ring-down time when analytes are in the cavity, and τ_0 is the ring-down time when no analytes are in the cavity.

When measuring using a CRDS as shown in Equation 2, the result is the extinction coefficient (α) of an analyte. It is an optical property of an analyte that equates to a light intensity decrease per distance traveled. Given a CRDS with a lower detection limit of 0.1 Mm^{-1} and an upper detection limit of 100 Mm^{-1} the following is an example of how extinction coefficient measurements could be interpreted for atmospheric measurements. An extinction coefficient < 1 Mm^{-1} means the analyte scatters or absorbs the incident light by a small amount over a megameter. An extinction coefficient > 100 Mm^{-1} means the analyte scatters or absorbs the incident light by a high amount over a megameter.

The ring-down time in Equation 2 partially depends on how the light couples into cavity modes.[6,7] Cavity modes are spatial patterns of oscillating light, created by interference within the cavity. The cavity modes determine many essential features of CRDS, such as the exponential ring-down time and how the light interacts with analytes. Slight alignment adjustments to the HR mirrors or reflectivity can have compounding changes on the ring-down time. Optimal cavity modes are where the pulsed light constructively interferes the greatest, creating the largest build-up of energy in the cavity given the cavity's physical parameters. The larger the energy built up, the longer the decay time out of the cavity. A feature that typically equates to an optimal cavity mode is exciting the TEM_{00} mode within the cavity.

Mirror contaminants such as water vapor and dust can become a severe problem for CRDS measurements because they can adhere to the mirrors and change their reflectivity, decreasing the

ring-down time.[7] To alleviate this problem a purge gas, such as nitrogen, flows over the mirrors. The flow rate of the purge gas is just enough to create a barrier between the mirrors and the incoming airborne analytes. The purge gas is also used to purge the cavity of any contaminates that might impact the following extinction coefficient measurements. A purged cavity is the baseline of the measurement and needs to be as clean as possible to provide accurate results.

This project focuses mainly on the environmental and chemical aspects of using a CRDS, but it is important to note its application in other sciences briefly. The same or a similarly modified CRDS design in this project could also be applied to astrophysics, biosensing, combustion, and material science.[7]

Astrophysicists have used CRDS systems to measure interstellar particles and gases.[7] Transient species that are usually unstable and are believed to be present during the formation and aftermath of celestial bodies are difficult to study. Besides being difficult to produce in a lab these molecules usually decay fast and are not produced in high quantities (10^7-10^{12} particles cm^{-3}).[7] CRDS systems successfully measure these molecules because of their sensitivity and time resolution.

CRDS has become a tool in biosensing applications to measure volatile molecules from exhaling.[7] Volatile molecules such as metabolites from exhaling are being studied as a means for detecting diseases and health problems. These molecules are airborne which make them perfect for CRDS systems since they excel at measuring airborne analytes and are sensitive enough to detect small amounts of the metabolites (ppm-ppb).[7]

In combustion research measuring the products from a combustion reaction is extremely valuable. Determining the products after a reaction and their properties is fundamental in all chemistry, the same ideology can be applied to combustion research. A CRDS can be installed inline with a combustion reaction to measure the products quickly without them changing states.[7]

CRDS systems can be used in materials science for measuring optical loss in optical components such as fiber optic cables.[7] After replacing the cavity with different optical components,

researchers can measure the difference in optical loss. In one study, they studied the optical loss of fiber cables of varying lengths and determined the loss was within the tolerance of what the manufacturer had stated.[7]

CRDS has many advantages and is used widely throughout differing scientific domains, but it still has some caveats. The main caveat concerns the limited wavelength range due to the laser and mirrors. Both the laser and mirrors used have to be rated to match a narrow wavelength range of each other. The highly reflective mirrors used for CRDS are reflective over only a narrow band of wavelengths (10-100 nm). The spectra of analytes are often challenging to measure because of the narrow wavelength range.

Low-Cost Aim

Low-cost instruments have been increasingly popular amongst hobbyists and home scientists, influencing low-cost adoptions in higher-level research.[8,9] The main attraction to low-cost instrumentation is paying far less for a product that meets the quality of a lab group's research goals. Instead of buying a costly instrument with multiple features a lab group would never use, one could buy or construct a low-cost one specializing in that group's research goals. With this in mind, researchers starting to get into a different research domain do not need to spend as much money to determine if that type of technique is worth further investment.

A popular example of home scientists using low-cost instruments is the PurpleAir™ air quality sensors.[10] These sensors are cheap $200-$300 and easy to set up to measure particulate matter at virtually any location. Even though these sensors are not Environmental Protection Agency (EPA) certified, there are more than EPA-certified devices, providing redundancy across huge areas. These sensors open up air quality research to people who cannot afford EPA-certified devices because of their cost and their publicly available data online. At Western Carolina University (WCU) alone there are 6 of these sensors at varying locations, consistently uploading their data for anyone to monitor online.

Another significant advantage of low-cost instruments is their ability to be constructed and

maintained.[9] Numerous commercial instrument problems stem from using proprietary parts and knowledge, which involves costly repairs. Low-cost instruments allow groups to cut repair costs and worry less about parts potentially becoming worn or broken. In atmospheric studies, instruments are often attached to airborne platforms such as weather balloons.[11] The instrument might be unrecoverable or break when coming back down; sending an inexpensive instrument can be cost-effective.

Project Goal

This project's main goal is to design and construct a low-cost CRDS that is comparable in performance to high-cost CRDS. To achieve this goal the first step is to develop a reduced cost CRDS by using off-the-shelf commodity parts instead of custom machined parts. After the reduced cost CRDS is constructed and tested the next step is to improve the design and reduce as many manufactured parts as possible with fused deposition modeling (FDM 3D-printing). Finally, the two designs would be compared to other CRDS to determine if these systems are viable in a research setting.

CHAPTER 2: MATERIALS AND METHODS

Sample Preparation

Acquisition of Samples

All samples used in this project except ambient aerosols were obtained through a manufacturer or generated in the lab. NO_2 was obtained through Airgas, and O_3 was generated in the lab using a Longevity Resources ozone generator. The ozone generator required $> 99.5\%$ O_2 which was sourced from Airgas along with liquid nitrogen from AndyOxy, the boiloff from which was used to dilute the samples and purge the cavity.

Ozone Preparation

The Longevity Resources ozone generator did not provide consistent ozone concentrations for the validation tests. Instead, an ozone trap was constructed to allow for finer control of ozone flow and dilution.[12,13] The trap consisted of a triple-valve glass vacuum trap, isopropanol, dry ice, silica gel, a dewar flask, and a vacuum pump. The silica gel was heated and dried in an oven at 100°C overnight ($>$ 8hrs). After drying and while warm, the silica gel was poured into the bottom part of the vacuum trap, almost filling the whole bottom part. The top part was promptly attached, ensuring a tight seal between both parts. Two valves were closed on the trap with only one valve remaining open with the vacuum pump connected to the open valve. The vacuum pump was turned on to remove residual contaminants from the silica gel. After an hour, the pump was turned off, and the valve was closed.

To trap ozone on silica gel with the lowest possibilities of hazards the silica gel temperature should be between -70°C and -100°C.[13] An easy way this was accomplished was by making a slurry of isopropanol and crushed dry ice contained within a dewar flask (-77°C). Once the slurry was prepared, the trap was lowered into the dewar flask using a ring stand as far as it could fit in a fume hood. The inlet and outlet valves on the trap were opened and the ozone generator connected to the inlet. Finally, the ozone generator was turned on to generate a high ozone concen-

tration and flowed through the trap. The ozone flowed through the trap until the top layer of silica gel turned dark blue/purple. Then, all the trap valves were closed, and the generator was disconnected.

Dislodging the ozone from the trap for measurement requires a carrier gas such as N_2. This process is similar to flowing ozone over the silica gel to trap the ozone, but ozone is removed from the trap and flows with the N_2. Having the three vales allowed for finer adjustments of flow rates through the trap.

Hardware, Data Acquisition, and Data Processing

Hardware

The CRDS hardware used in both CRDS designs is shown in Table 1. Both CRDS designs are not dependent on using this hardware, but this project focused on acquiring data at 445 nm and therefore required sourcing parts for that wavelength; laser, mirrors, optical isolator, achromatic lens, and detector. The other hardware is not necessary for 445 nm measurements and instead was sourced due to availability or specific technical properties.

Program Framework

Custom programs written using Julia,[14] Python,[15] and C++ were used to acquire, process, and display the data. Using open-source software reduces the cost of the instrument and allows us to have full control over how data acquisition, processing, and presentation are handled.

Data Acquisition

A photodiode was positioned at one end of the cavity to detect the light intensity over time after exiting the cavity. The electrical signal from the photodiode was digitized with an oscilloscope. The oscilloscope acquired the data at 25 MSa/s with each captured waveform amounting to 70 k points. An external device can then query the waveform that the oscilloscope acquires. The external device, such as a minicomputer, runs a Julia/Python script that acquires, processes, and displays the data. The Python portion of the script queries a captured waveform on the oscilloscope every 4 seconds through a transmission control protocol (TCP) connection. The Python portion

Table 1. CRDS Hardware

Component	**Model**
Laser	OBIS™ LX 445 nm (Coherent, Inc)
Optical Isolator	Thorlabs™ IO-3D-440-PBS
Mirrors	FiveNines Optics T = 37 ppm @ 445 nm, PL-concave, R.O.C = 25 cm
Achromatic lens	Thorlabs™ TRH254-040-A-ML
Detector	Thorlabs™ Avalanche Photodiode APD410A
Oscilloscope	Siglent™ SDS1204X-E
Development Board	Teensy™ 4.1 (PJRC, Inc) + Ethernet Adaptor + BME680 Sensor
Data Processor	GMKtec™ Nucbox 8
Ethernet Switch	TP-Link™ TL-SG105E

of the script also queries a development board for data through a TCP connection. The development board has a BME680 sensor (Bosch/Seeedstudio) that appends the temperature, humidity, and pressure data after every query into a CSV file.

Data Processing

Once the oscilloscope receives the waveform (Fig. 3.3), the Julia portion of the script separates the waveform into individual decay events, fits the data of each decay event using Equation 3, and averages the exponential decay constants from each fit.

$$I(t) = I_0 e^{\left(\frac{-t}{\tau}\right)} \tag{3}$$

$I(t)$ is the intensity of light at a specific time in the decay, I_0 is the initial intensity of light of the decay, t is the time at which $I(t)$ is measured, and τ is the time it takes for the light intensity to reach $1/e$ or 37% its original intensity.[16]

The LsqFit.jl[17] package for Julia was used to fit each exponential decay; the package uses the Levenberg Marquardt algorithm at the time of writing. The following code block is the Julia code for calculating the exponential fits. LsqFit.jl uses the model displayed in the first line of the following code block to fit each exponential decay using the total time of each decay event (`time`), the waveform data (`m2`), and the guess values in an array (`p0`). After fitting the ring-down time for each decay event, the values of τ in an array are averaged together. The standard deviation is also calculated based on those values of τ.

```
crd_model(t, p) = p[1] * exp.(-t / p[2]);


function fitCRD(waveform::Vector{Float64}, n::Int64, startpt::Int64, endpt::
    Int64; s, model = crd_model, p0 = [0.08, 7.5])
try
    m = reshape(waveform, :, n) # reshape
    r = reshape(waveform, :, n)
    m2 = m[1:endpt, :] # discard second half of period
    r2 = m[1:endpt, :]
    time = Array(1:1:size(m2)[1]) .* s^-1 .* 1e6 # compute time values
    τ = ones(Float64, n) # pre-allocate τ array
    A = ones(Float64, n)# pre-allocate A array
    for i in 1:n
        m2[:, i] = m2[:, i] .- mean(m2[(endpt-300):endpt-100, i]) # baseline
            correct
        nlfit = curve_fit(crd_model, time, m2[:, i], p0); # fit
        τ[i] = nlfit.param[2];
        A[i] = nlfit.param[1];
        r2[:, i] = nlfit.resid
    end
    return (τ = τ, A = A, data = m2, t = time, n = n, resid = r2)
catch
    println("fitCRD Fail")
end
end;
```

There are a few important features within the main function that was written to fit the data. The main calculation code block is contained within a try/catch block. This ensures that even if an error occurs during processing it does not halt the program script and lets it continue to try again. Each decay event (period) is separated based on the frequency of the trigger and the sampling rate of the oscilloscope. With these two variables, the points per period can be calculated to determine how many points each decay event amounts to. The second half of the period is discarded to remove the waveform parts that equate to the laser turning back on, ensuring a clean exponential decay to fit. The `time` is the sampling rate converted to seconds over the length of the `m2` array. Finally, a simple baseline correction is employed in the `m2` array to ensure the decay event ends close to zero intensity so the function can accurately calculate the ring-down time (τ).

CRDS Data Processing Caveats

When fitting the decay events from a CRDS, there are unique caveats that need to be approached depending on hardware and software. Some of these problems, such as the discarded second half of the decay event and baseline correction, were mentioned earlier. Other problems that need resolution usually come from the oscilloscope itself or certain variables in the script that is unique to different acquisition parameters. Three important situations to consider are the starting point of the first period, the visibility of the waveform being captured, and the number of points per waveform capture.

The starting point of the first period determines how the separated event periods will be fitted since a set amount of points per period breaks them up. Our starting point was 1885, and the horizontal scale on the oscilloscope was always set to zero, so the starting point never needed to change afterward. The vertical scale of the oscilloscope determines how compressed or stretched the waveform is after capture. A heavily compressed waveform will not fit properly since there is insufficient vertical data to fit the decay. Being too stretched can potentially eliminate the top and bottom waveform points by going beyond the capture screen. This usually is not a problem when

displaying the waveform. Sometimes when aligning the mirrors and purging with N_2, the intensity of light passing through the cavity can increase, pushing the top and bottom of the waveform past the capture display. Finally, the number of points per capture relates directly to how many points are used per fitting. Having enough data points per decay event is crucial, which is why it is important to use an oscilloscope that has the right acquisition features. Our oscilloscope captured 20 full decay events with our parameters which means there were $\sim$3333 points per period, and since half of the period was removed only $\sim$1666 points were used per period and fitting. These were enough points to enable proper fitting; anything under 1000 pts per period caused some fitting problems. Fewer data points per period equated to a greater standard deviation in the final average since a few points in each decay could change the fitting by a marginal amount. This could be mitigated by having fewer decay events per capture; 20 events was the sweet spot. Additional decay events could have been captured if the memory depth was increased, but the next setting was 700 k points, which made the data acquisition and processing longer.

Data Storage

After the data acquisition and processing the time at acquisition, average ring-down time (τ), average ring-down time standard deviation, temperature, barometric pressure, and relative humidity are stored in a comma-separated-value (CSV) file. Each query amounts to 6 data points, which are stored in separate columns in the same row. Additional data queries are appended as new rows to the file.

Graphical User Interface

A graphical user interface (GUI) was designed to start/stop the data acquisition and processing, name files and access them, and observe the ring-down time in real-time (Fig. 2.1). The GUI was coded using Julia with the Genie Framework.[18] This framework is oriented toward building interactive and reactive data science web pages. Executable style GUIs such as GTK were previously used but caused many problems, especially with accessibility across different operating systems.

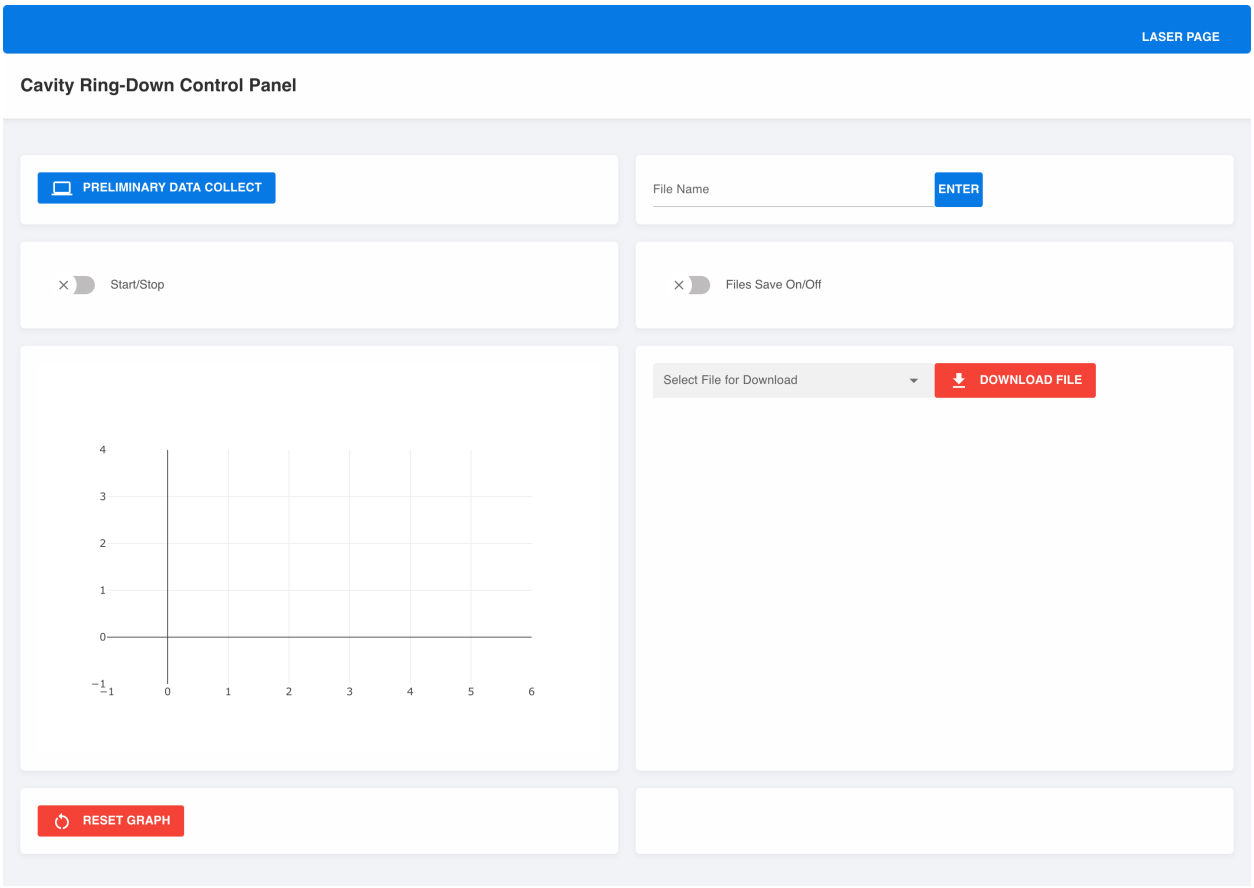

Figure 2.1. CRDS GUI main page without any data or components enabled.

The minicomputer hosting the Julia/Python programming script has the GUI portion within the script. The GUI can be accessed remotely by connecting the minicomputer to a network and using the available IP and port. If the computer running the programming script is not on a network, then the GUI will open on a default browser and be accessible only on that computer. The network method allows multiple users to access the GUI simultaneously if they can connect to the same network.

Once connected, the web page is interactive and reactive, meaning any input to the GUI reacts with the Julia/Python script controlling the data acquisition and processing. This reactivity also allows multiple users to see the same information displayed such as plots, file names, and

indicators that the script is acquiring and processing data.

The main components of the GUI are data file selection and downloading, data acquisition and processing start/stop buttons, process indicators, a plot displaying real-time data of the ring-down time over time, and a laser control panel. File names can be easily written in a text input that reflects the name of the final data file being saved. After the first bytes of data are saved to the data file, it can be selected from a drop-down menu that displays all files in a data file directory. Any file selected can be downloaded after a measurement is complete or during, allowing for data post-processing during a measurement. A toggle button starts/stops the data acquisition and processing portion of the code, and since it is reactive, other users can see if it is running. The plot displaying the ring-down time over time is also synced across users, with a reset button when new measurements are taken. The laser control is a separate page from the main web page and allows the user to control all laser functions through buttons and serial commands. It requires a serial connection to the minicomputer which the Julia script can send serial commands through.

Instrument Performance

When testing the performance of an instrument an Allan deviation analysis can be utilized to determine the drift, the ultimate limit of detection (LOD), and optimal averaging time.[19,20] Allan deviation calculations were done using the Julia package AllanDeviation.jl,[21] which uses the equations from Riley et al.[22]. An Allan deviation is similar to a standard deviation calculation except it measures variability over time. This is useful for measuring the deviation over time to observe drift during measurements. Drift happens in all instruments so measuring it allows one to potentially tune out problems and ensure measurements drift a minimal amount.

Calculating our Allan deviation started with instrument measurements in an optimal environment without any analyte being measured. Since it is in an optimal environment, the elements of an Allan deviation should be viewed as a best-case scenario and a guide to moving forward. Calculating an Allan deviation using data points measured in a sub-optimal environment creates problems with pinpointing variables in the instrument causing underlying problems. An optimal

environment is temperature and humidity controlled and will not interfere with the instrument's measurements, such as vibrations from foot traffic or stray light interference.

While Allan deviation is useful in determining the drift of the instrument, the LOD it provides is unrealistic because of how data processing is handled during measurements. In atmospheric measurements, the instruments are sampling for continuous intervals and require blank measurements (τ_0) to occur during the sampling periods.[23] To calculate a more realistic LOD, the data from the Allan deviation measurements are separated into intervals to mimic real measurement intervals. These intervals are based on the optimal averaging times from the Allan deviation calculations. The data is divided into 30 minute intervals with a 2 minute blank (τ_0) and a 28 minute sampling period (τ). This is equivalent to taking a new background every 30 minutes and using that new background to calculate the following sampling period. These 30 minute intervals are then appended together to create a data set that mimics real data measurements. After the data is replicated into realistic measurements, the actual LOD of the instrument can be determined using the 2σ method. A similar method was used in Fischer and Smith[23] where they had a 662 nm CRDS, and in Nakayama et al.[24] but used a photoacoustic soot spectrometer and a photoacoustic extinctiometer.

CHAPTER 3: CRDS DESIGN AND PERFORMANCE

As mentioned before, low-cost instruments are becoming more popular among scientific groups. The main draw to these instruments is their ability to be assembled from non-proprietary parts, and to design the instrument to meet specific criteria for a group. As an example, a specific criterion for our group's CRDS was its ability to be used to calibrate a photoacoustic spectrometer (PAS) that samples ambient aerosols. In this project two CRDS configurations were developed; one involving primarily ThorLabs™ parts (Kinematic System), and another using fuse deposited printing to create a cage system and mounts (Cage System).

Kinematic System

Design

The first CRDS design involved mainly manufactured parts. These parts were sourced primarily from ThorLabs™ besides some components in Table 1. Since none of the parts are machined (except for some drilled inlet and outlet holes), the CRDS could be assembled quickly, and the design could be altered easily if needed.

The starting point of this CRDS design was using 3-adjuster kinematic mounts from Thorlabs™ (PN: KS1T). Since the mirrors require a high level of tuning to optimize the cavity mode these seemed like they would give a great amount of tunability and are commonly used for CRDS instruments. These mounts had SM1 female threads so that SM1 lens tubes and fittings could be attached. To properly use the kinematic mounts, the cavity requires a flexure point between the two mounts. A flexible PTFE bellows from ThorLabs™ (PN: SM1BTK) was connected to both cavity sides to create a flexure point. The bellows had KF25 fittings on each side and were sealed to the lens tubes by KF25 adaptor fittings that threaded into both male and female threads. So the cavity is kinematic mount $\rightarrow$ lens tubes $\rightarrow$ bellows $\rightarrow$ lens tubes $\rightarrow$ kinematic mount, as shown in Figure 3.2.

The laser, optical isolator, cavity, and photodiode were mounted on one movable optical bread-

board. The laser, along with a heatsink, was mounted directly to the breadboard with stainless steel spacers to adjust the height. The isolator was mounted to the breadboard by a Ø1/2" pedestal post. The cavity was mounted by bolting stainless steel pedestal pillar mounts to both kinematic mounts. The photodiode was mounted to the breadboard by a Ø1/2" pedestal post. All four components were not directly connected; they were aligned at the same height in a straight line on the breadboard. Other components, such as the laser controller and development board, were mounted on the breadboard but are not crucial to the CRDS optical design. The optical breadboard has 4 vibration isolating feet (ThorLabs™ PN: AV4) on each corner to help reduce vibrations.

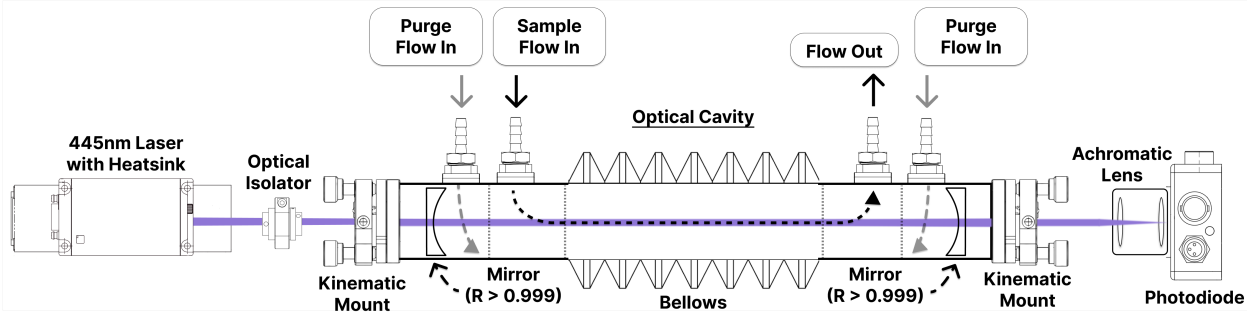

Figure 3.1. Block diagram of the kinematic system CRDS.

This CRDS cavity still required inlet and outlet ports for the purge gas and sample flow. To accomplish this four holes were drilled in lens tubes. Two holes were 1/16", the other two were 1/4" in diameter, and all four were approximately midway in each lens tube. The holes were fitted with 3" length Ø1/16" and Ø1/4" stainless steel tubes, making sure the tube did not encroach on the inner lens tube threads. The tubes were secured with two-part epoxy (JB Weld) for several hours. The lens tubes that had the Ø1/16" steel tubes were threaded closest to the kinematic mounts, and the lens tubes with the Ø1/4" steel tubes were threaded closest to the bellows. The purge flow lines were connected to the Ø1/16" ports, which also were the lens tubes that would

house the HR mirrors. The sample flow lines were connected to the Ø1/4" ports (Fig. 3.1).

To finish constructing this CRDS, the HR mirrors had to be placed in the lens tubes directly connected to the kinematic mounts. A Ø1" o-ring was placed in first, followed by the mirror, then a retaining ring. The retaining ring was tightened slowly onto the mirror, applying just enough pressure to create a seal between the o-ring and the mirror, and not allowing any movement. To seal the cavity properly, each SM1 thread was wrapped in PTFE tape before being assembled together. Once everything was ready, the lens tubes were screwed in, bellows attached, and then PTFE plastic tubing placed onto the inlet and outlet ports. To keep the mirrors clean, the sample inlet port was plugged, and the cell was purged with 40 standard cubic centimeters per minute (SCCM) N_2 through the purge gas lines, keeping moisture and contaminants out of the cavity. There was a concern that the cavity would not be airtight because the SM1 threads do not create an airtight seal, but the PTFE tape created a sufficient seal. The seal of the cavity was tested with soapy water.

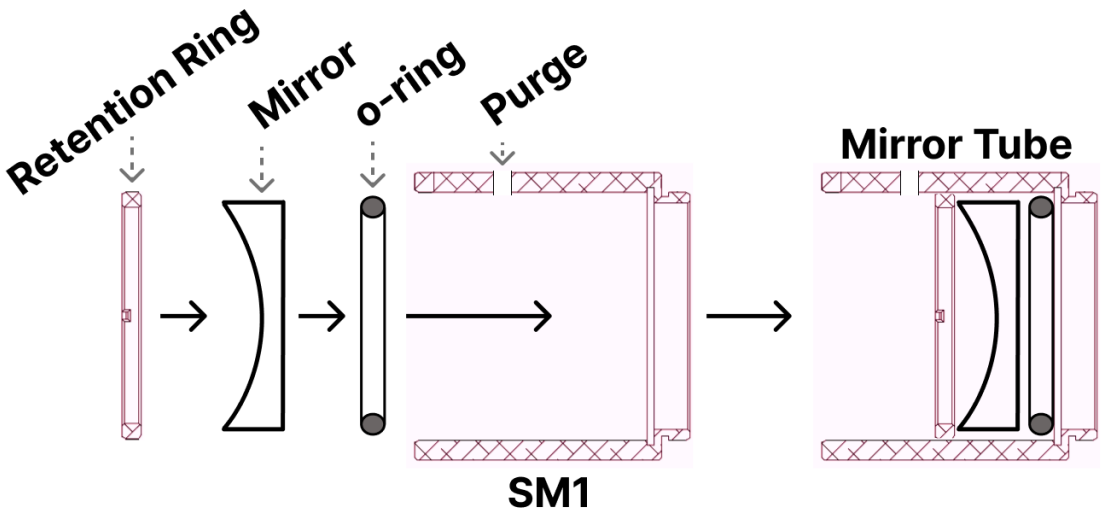

Figure 3.2. Block diagram of an SM1 lens tube that houses an HR mirror for the kinematic system.

Alignment Process

When starting the optical alignment of the CRDS, the laser and optical isolator were aligned at the same height, to where the laser beam passes through the isolator. Afterward, the isolator is slightly rotated on the z-axis to ensure the laser back reflection does not reflect directly into the laser. This step might also require the pillar mount to be moved slightly to compensate for the rotation of the isolator. Next is aligning the mirror closest to the photodiode (back mirror) with the optical isolator. The back mirror kinematic mount is adjusted to where the light reflecting off the back mirror now transmits through the isolator. After the back mirror alignment, the front mirror is put into the cavity. With the same action as the back mirror the front mirror is adjusted so the reflecting light transmits through the isolator.

The next step for aligning this CRDS is aligning the photodiode and tuning the kinematic mounts so that an optimal cavity mode can be obtained. The kinematic mount tuning was the most recurring step in the optical alignment of the CRDS before measurements. First, the photodiode with the achromatic lens attached is made sure to be pointed toward the back mirror and centered vertically respective to the mirror. The photodiode should be connected to the oscilloscope with the development board modulating the laser and acting as a trigger for the oscilloscope. With the laser at full power, a waveform should appear on the oscilloscope similar to Figure 3.3.

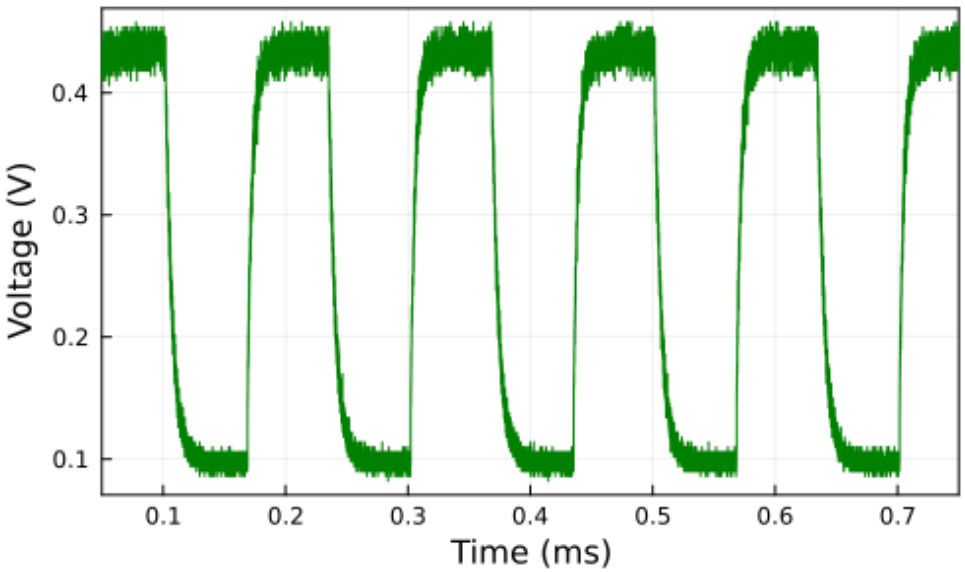

Figure 3.3. Plot showing how multiple ring-down events would be measured by an oscilloscope.

Once a waveform similar to Figure 3.3 appears then adjustment of the kinematic mounts and photodiode can be optimally tuned. The kinematic mounts were tuned one at a time, turning each knob on the kinematic mount slowly, and watching the oscilloscope for changes. An increase in the intensity of the waveform can correlate to a longer ring-down time but can be unreliable. That is why once a proper waveform is achieved the minicomputer running the data acquisition script can be used to measure the ring-down time reliably. When tuning the mounts produces no greater increase in ring-down time then measurements began.

Performance

For the kinematic system Allan deviation tests, the CRDS was placed on an optical table in a laser lab at WCU. This laser lab had semi-optimal conditions such as vibration dampening and laser curtains for stray light. The sub-optimal conditions were that the building would undergo abrupt temperature swings to regulate the humidity. Even with the temperature swings the room provided a satisfactory environment for conducting Allan deviation measurements.

After completing multiple measurements and calculating their Allan deviation, it was appar-

ent that there was substantial day-to-day drift in the instrument. Many times the measurements could not be used for an Allan deviation calculation because of the drift. Figure 3.4 has both extinction coefficient (α) measurements and temperature measurements of the kinematic CRDS over 19 hrs.

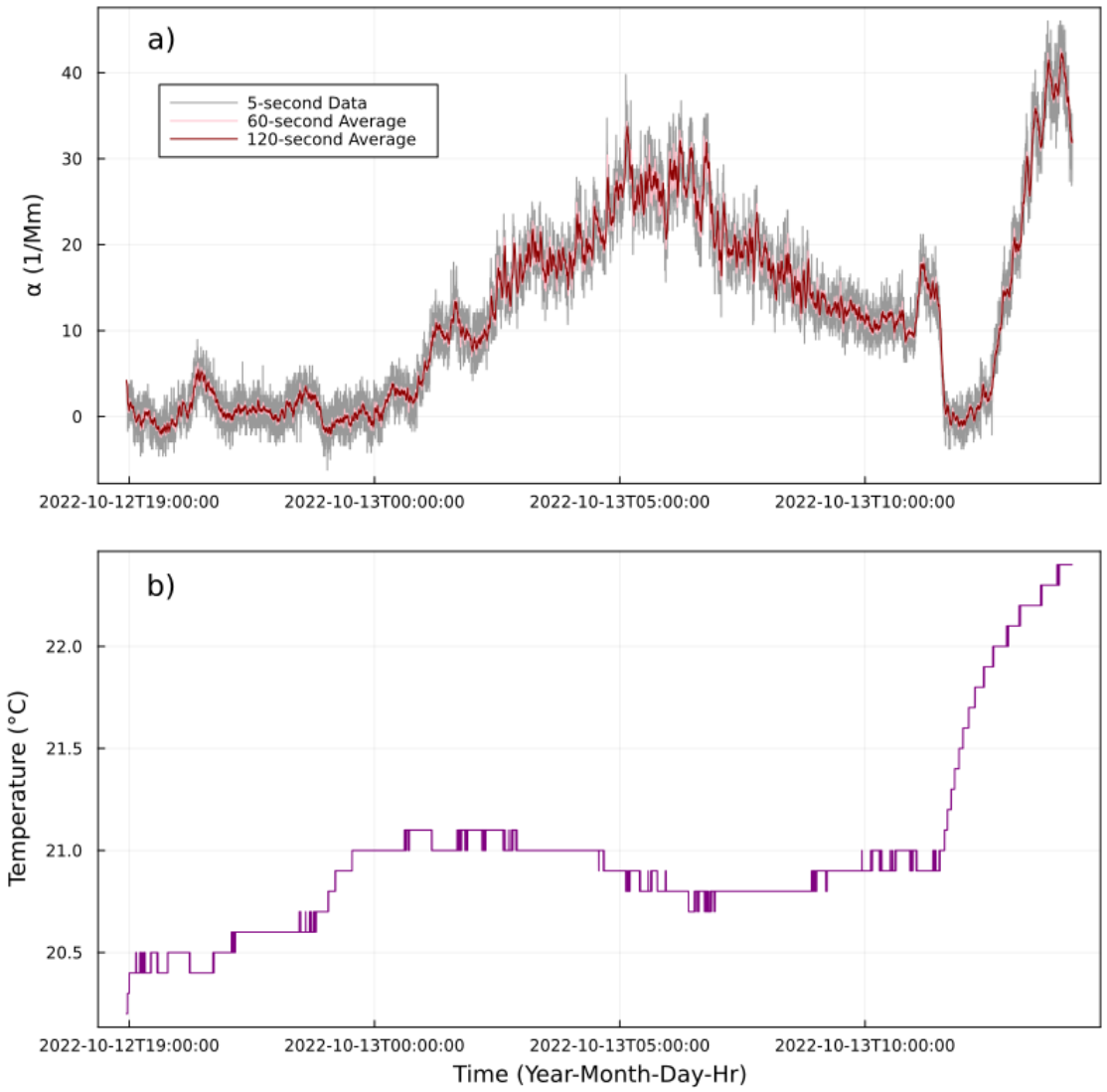

Figure 3.4. Extinction coefficient and temperature measurements of a N_2 background using the kinematic system (10/12/22 - 10/13/22)

A couple of things are apparent in the data, firstly the extinction coefficient drifts egregiously. Figure 3.4 also has a corresponding temperature graph that shows that the measured temperature shares a similar shape to the measured extinction coefficient. This was the first indication that the temperature in the lab room was inconsistent and produced drift in the measured extinction coefficient. Calculating an Allan deviation using this data (Fig. 3.5) shows the apparent drift in the instrument clearly. The ultimate LOD was 1 Mm^{-1} at an optimal averaging time of 80 s.

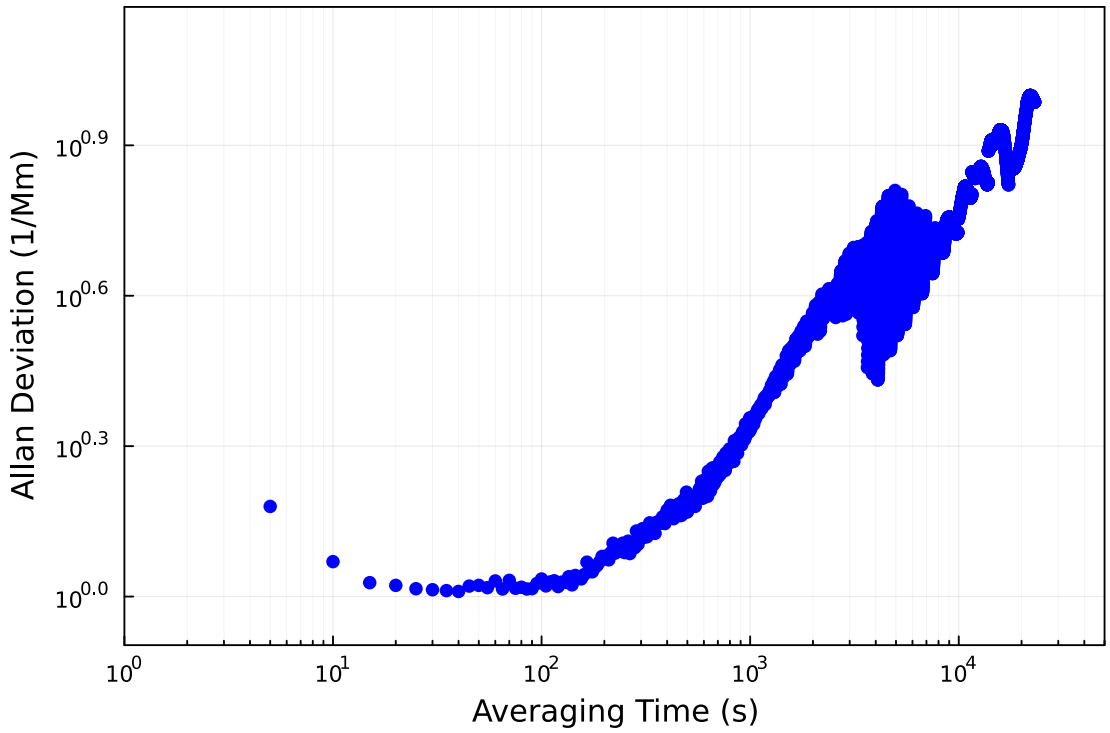

Figure 3.5. Allan Deviation of extinction coefficient using kinematic system data from Figure 3.4

Compared to other Allan deviations this plot shows very little decrease initially. This means the LOD of the instrument is limited entirely by drift and shows very little influence from random noise. This and many other measurements on this instrument point to a likely correlation between the extinction coefficient and temperature. This is a huge problem as the majority of atmospheric

measurements take place in environments where temperature is not controlled. Increasing the performance of the instrument and determining what variable was causing these problems was key.

To determine the likely cause of drift each component of the CRDS was examined and adjusted to see if it improved performance. After various tests, the kinematic mounts seemed to be the greatest contributors to drift. The kinematic mounts are tensioned by small steel springs. These springs likely compress and expand due to temperature changes. These changes are small but change the mirror angles enough to cause drastic problems.

The best method for minimizing this drift was adjusting the kinematic mounts so that the two plates were close together, decreasing the tension of the springs. Figure 3.6 represents measurement data with the new kinematic mount method. There is still a slight correlation between the extinction coefficient and temperature, but the extinction coefficient variability decreased heavily compared to 3.4. The extinction coefficient variability is closer to the ideal value 0 Mm^{-1}.

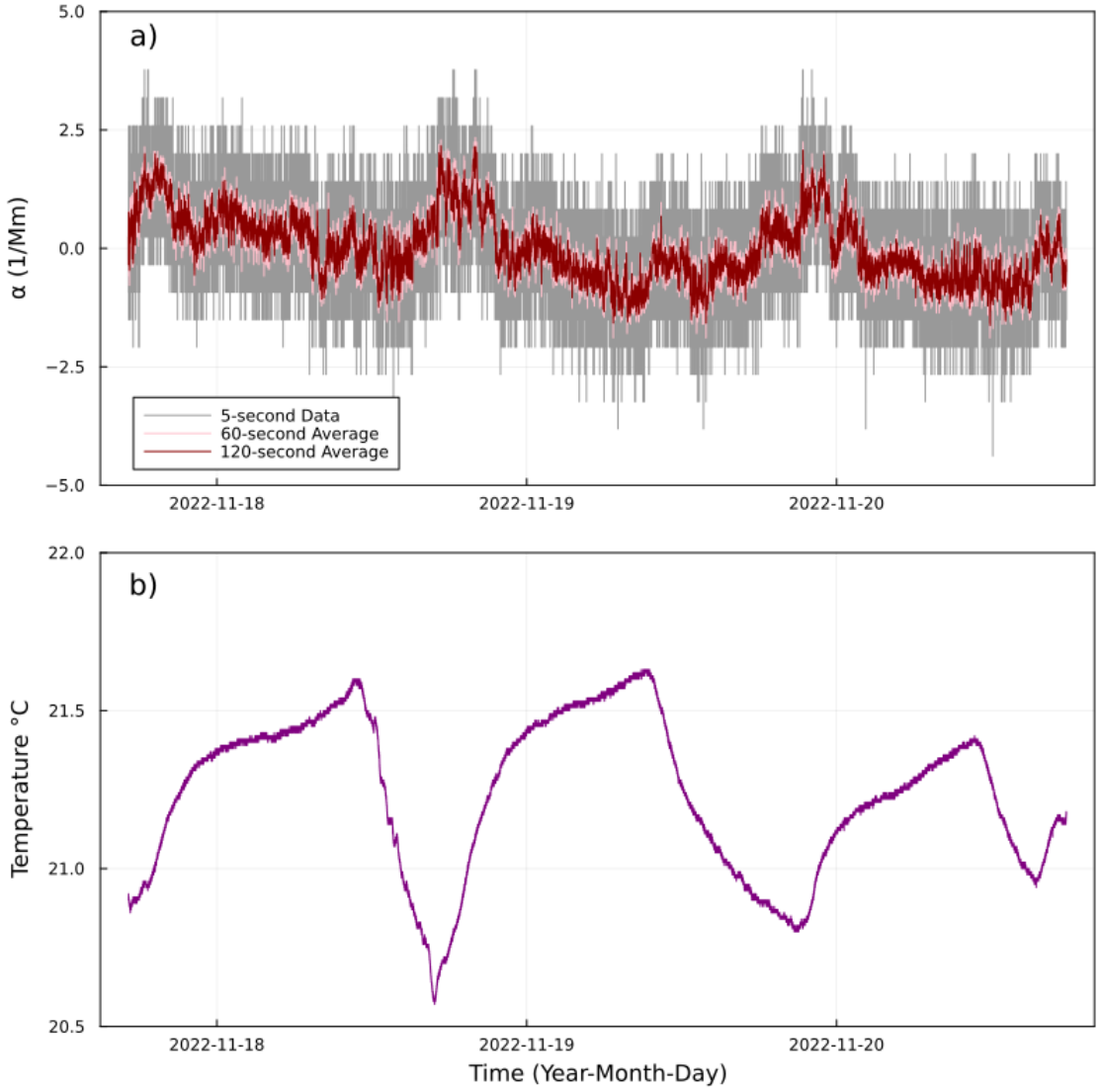

Figure 3.6. Extinction coefficient and temperature measurements of a N_2 background using the kinematic system with slight adjustments (11/18/22 - 11/20/22).

Using this measurement data to calculate an Allan deviation also showed increased performance and stability (Fig. 3.7). The ultimate LOD was 0.2 Mm^{-1} at an optimal averaging time of 324 s. Even with these improvements, in subsequent measurements the success of an Allan deviation calculation varies, which was also a problem before the improvements.

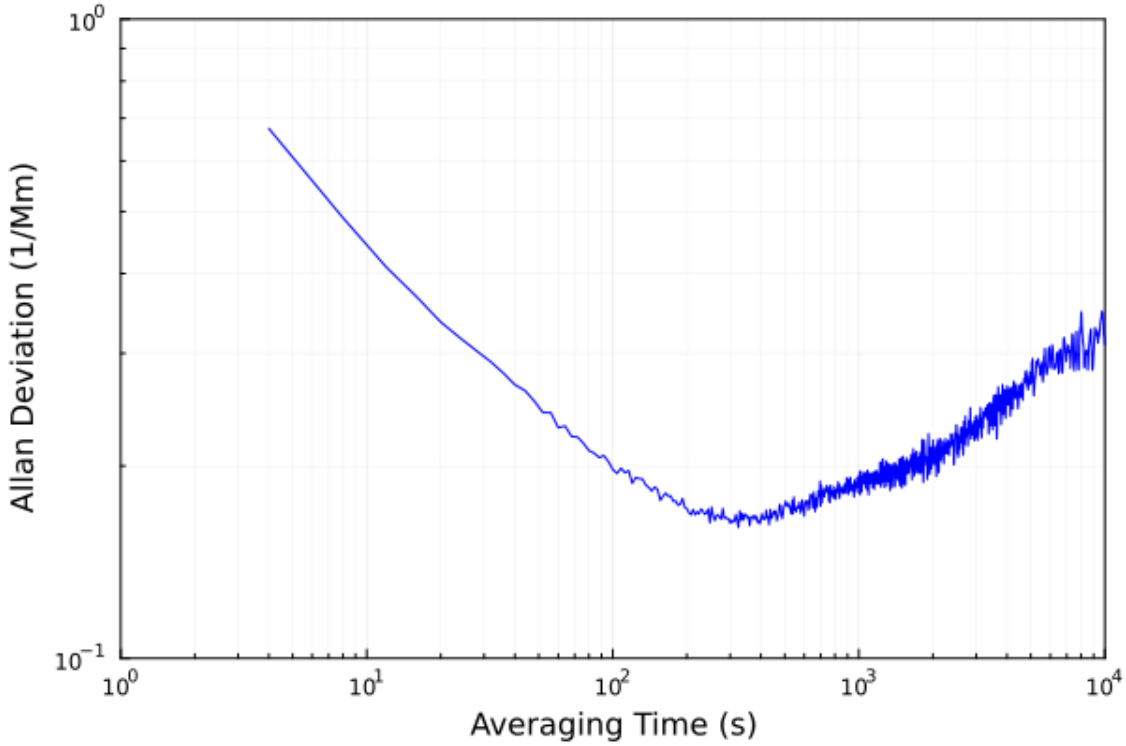

Figure 3.7. Allan Deviation of extinction coefficient using kinematic system data from Figure 3.4

Table 2 shows a complication spread of kinematic Allan deviations results. These results include those displayed earlier and another successful result. More measurements were conducted, but oftentimes the results produced Allan deviations that were incomprehensible. From this table, the standard deviation of the LOD and optimal averaging time are also calculated and presented. This gives a general overview of the performance of the kinematic system and will be used comparatively later against the cage system.

Date	LOD	Avg. Time
2022-10-12	1.0 Mm^{-1}	80 s
2022-10-18	0.44 Mm^{-1}	234 s
2022-11-18	0.16 Mm^{-1}	324 s
Mean	0.53 Mm^{-1}	212 s
SD	0.43 Mm^{-1}	123 s
RSD	80.2 %	58.0 %

Table 2. Kinematic system Allan deviation results tabulated, with the mean, standard deviation (SD), and relative standard deviation (RSD) of the ultimate LOD and optimal averaging times at the bottom.

Figure 3.8 is the calculated 30 minute interval separation from Figure 3.6. The realistic LOD was calculated to be 1.6 Mm^{-1} with no time averaging using 2σ. The data here tells more about how the LOD would be if measuring atmospheric conditions. The CRDS constructed by Fischer and Smith[23] uses a 662 nm CRDS, and their realistic LOD is a couple of magnitudes better at 0.54 Mm^{-1}.

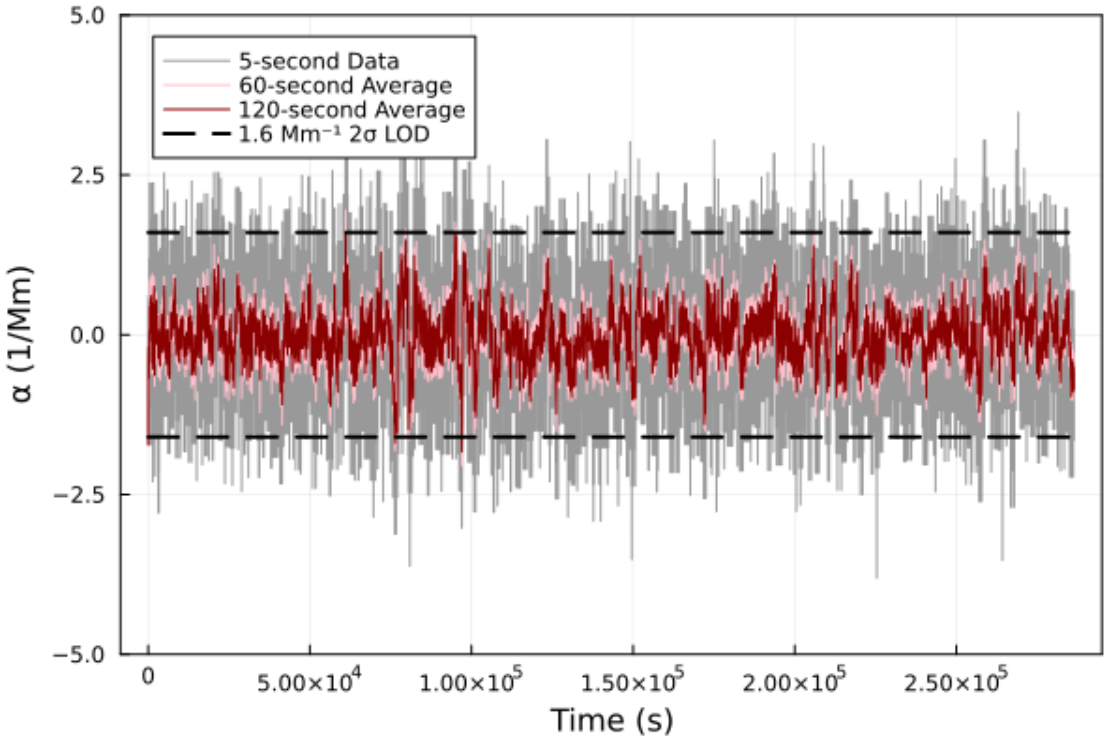

Figure 3.8. Calculated 30 minute interval separation from Figure 3.6 collected by the kinematic system.

Cage System

Design

The cage system uses the major components of the kinematic system such as the laser, optical isolator, mirrors, achromatic lens, and photodiode. The major difference between the two is that most of the mounts are produced by fused deposition modeling (FDM), and the system is mounted on 3 Ø1/2" carbon fiber rods. The orientation of the cage has the carbon rods in an equilateral triangle formation (Fig. 3.9). The main purpose of this design was to eliminate the kinematic mounts used in the previous design since some correlations between temperature and ring-down time were observed (Chapter 4). This design is similar to cage systems that have been done before but those cage systems have custom machine or high-cost parts.[25,26] Cage systems

for optics and CRDS systems work exceptionally well, and creating something similar would likely eliminate performance problems the kinematic system CRDS was having.

The mirror mounts were the most crucial component of the cage system since mirror alignment is crucial for coupling into optimal cavity modes and increasing the instrument's resolution. Other CRDS systems use static mirrors, which means once they are adjusted and aligned, they are made to never move again. The advantage of this is a decrease in drift that could originate from fluctuations in mirror alignment. The mirror mount design follows a similar static design and maintains mirror alignment by fastening the mount in place. This differs from the kinematic mounts used in the kinematic system as they maintain the alignment of the mirrors using springs. The mirror mounts needed a place to hold the mirrors, purge inlets, and a connection point for the sample flow inlet and outlet components.

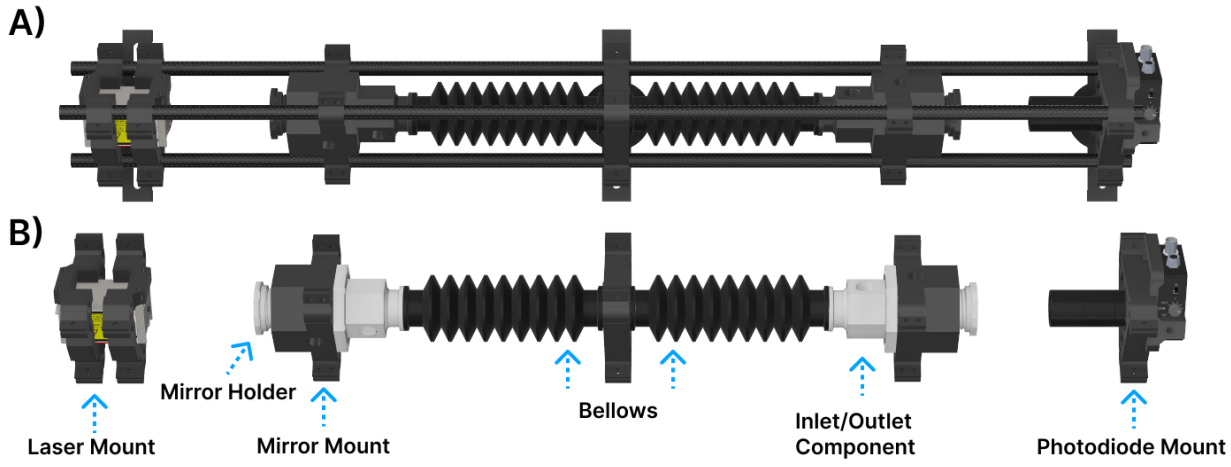

Figure 3.9. Block diagram of the kinematic system CRDS. A) Complete cage system. B) Cage system with the carbon rods removed and labeling of parts.

A simple way to achieve the static nature of the mirror mounts was creating a bolt-like design that screwed into the mount and held the mirror against the mount. The bolt was dubbed the mirror holder and is hollow straight through, allowing the laser light to pass through. The mirror

mount has threads for the mirror holder, and when the mirror holder is threaded in along with the mirror, it has a static x-ring (McMaster-Carr™ PN: 6540K251) to seal the mirror against the mirror mount. x-rings are similar to o-rings except they have an x-shape and have twice the sealing surface and require less squeeze to seal comparatively. These features are great for optics such as mirrors since this enables proper sealing with less worry about slightly uneven pressure and surfaces. The outer part of the mirror mount has rod clamps at its corners, forming a triangle so that the carbon rods can be pushed through them. The rod clamps have M4 nut and bolt holes so the mount can be tightened onto the rods, securing them in place. The rod clamps are also slightly larger in diameter compared to the rods, giving them some room for angle adjustments. For even finer adjustments alone, rod clamps that could fit around the rods were made and placed on the sides of the mounts, allowing the mirror mount to be set in a certain orientation other than just being tightened to the rods. These follow a similar design to the post collars provided by ThorLabs™ (PN: R2), and some were used on the cage system to test their performance.

On the bottom/flat side of the mirror mount, there are six M4 female threads and an o-ring placed into a circular slot. A separate FDM component that contains inlet and outlet fittings is attached to the mirror mount where the o-ring sits. This was done so that one large piece did not need to be FDM printed in one body with huge amounts of support material. This component had 1/8" FNPT threads for inlet and outlet fittings, KF25 flanges for quick connectors, and KF25 fittings to connect to PTFE bellows from ThorLabs™. The two sides of the CRDS are connected with bellows, but future designs will aim to eliminate the bellows and use a stainless steel tube instead.

Multiple tests were conducted in a water bath to test the seal of the FDM parts. The FDM parts were submerged in a water bath with a pressure gauge attached at one of the inlets, a purge connection at another inlet, and the rest of the holes sealed. Once submerged the parts were pressurized to 40 psig with N_2. After the pressurization, the gauge was inspected along with any bubbles leaking from the FDM parts. The gauge inspection gave a rough estimate of what pressure

the FDM parts could handle before heavy leaks. If N_2 was leaking from an FDM printed part, it was inspected further, and the FDM print settings were changed to improve its leak resistance. The bottom side of the inlet mounts often had small grooves from the FDM printing and required sanding to make it smooth to seal properly. After multiple rounds of testing and revisions, the seal between the mirror mount and inlet/outlet component was airtight until $\sim$10 psig, which is sufficient since the cavity is usually at atmospheric pressure.

Some FDM slicer settings that proved more useful in creating a more airtight/sturdier part were wall thickness, top/bottom thickness, stringing prevention, slower printing speed, and infill pattern. Wall thickness refers to how many layers of layer printing will occur. More walls mean that if one wall layer is faulty, another can patch that fault. The top/bottom thickness is the same premise as the wall thickness, but this is how many solid layers are printed at the top and bottom of the object. Stringing occurs when the nozzle of the FDM printer is too hot, causing the filament to string like a cobweb over time. This makes cleaning the part harder, and it is usually also indicative of other problems that the print will have, like nonuniform filament forming around the print. Slowing the print speed allows the filament to properly cool and harden before the next layer is deposited on top; PETG filaments usually need a slower print speed to allow more cooling time, while PLA does not need the same settings. An infill pattern is how the space between the walls is printed. Some infill patterns that seemed to work the best were those that created many subdivisions such as tri-hexagonal, or gyroid.

Alignment Process

Almost every calibration step used for the kinematic system applies to the cage design. The mirror mounts are really the only thing that required calibration since all other pieces are mounted to the cage system. The photodiode, for example, does not need its height adjusted or slightly turned since the detector mounts in the center facing the back mirror.

The mirror mounts have a small rod clamp gap to allow for movement as mentioned earlier, which allows them to be angled slightly. Instead of adjusting knobs, these mounts are ad-

justed by angling them directly and then securing them in place. Adjusting the mirror mounts and looking at the oscilloscope simultaneously works for this design too. When adjusting the mirror mounts, one mount was adjusted and locked in place by separate rod clamps, and then the other mount was adjusted, going back and forth between mounts until an optimal ring-down time was achieved.

Performance

The cage CRDS Allan deviation tests were conducted in the same environment and manner as the kinematic system. After completing multiple measurements and calculating their Allan deviation, drift problems were observed, but not as substantial as the kinematic system. Figure 3.10 shows one of the multiple measurements conducted for the Allan deviation calculation. Figure 3.10 has both extinction coefficient measurements and temperature measurements of the cage system CRDS over 46 hrs.

Looking at the data in Figure 3.10 there is less of an extinction coefficient deviation compared to Figure 3.4 but a worse drift from start to finish compared to Figure 3.6. The extinction coefficient levels out as time progresses, so the start of the data might be due to contamination on the mirrors that are removed over time or warming up of the hardware. The temperature data during the same time also depicts less correlation between the two. What noticeably correlates between the extinction coefficient and the temperature are abrupt mini fluctuations. This has never been observed before in any of the measurements until an Alicat™ mass flow controller was used to maintain constant flow as opposed to the needle valve used previously. Whatever is causing the mini temperature fluctuations is likely causing subsequent fluctuations in the extinction coefficient. While these fluctuations are small, they are abrupt and add to the drift of the measurements, which is why in Figure 3.11 there are two dips.

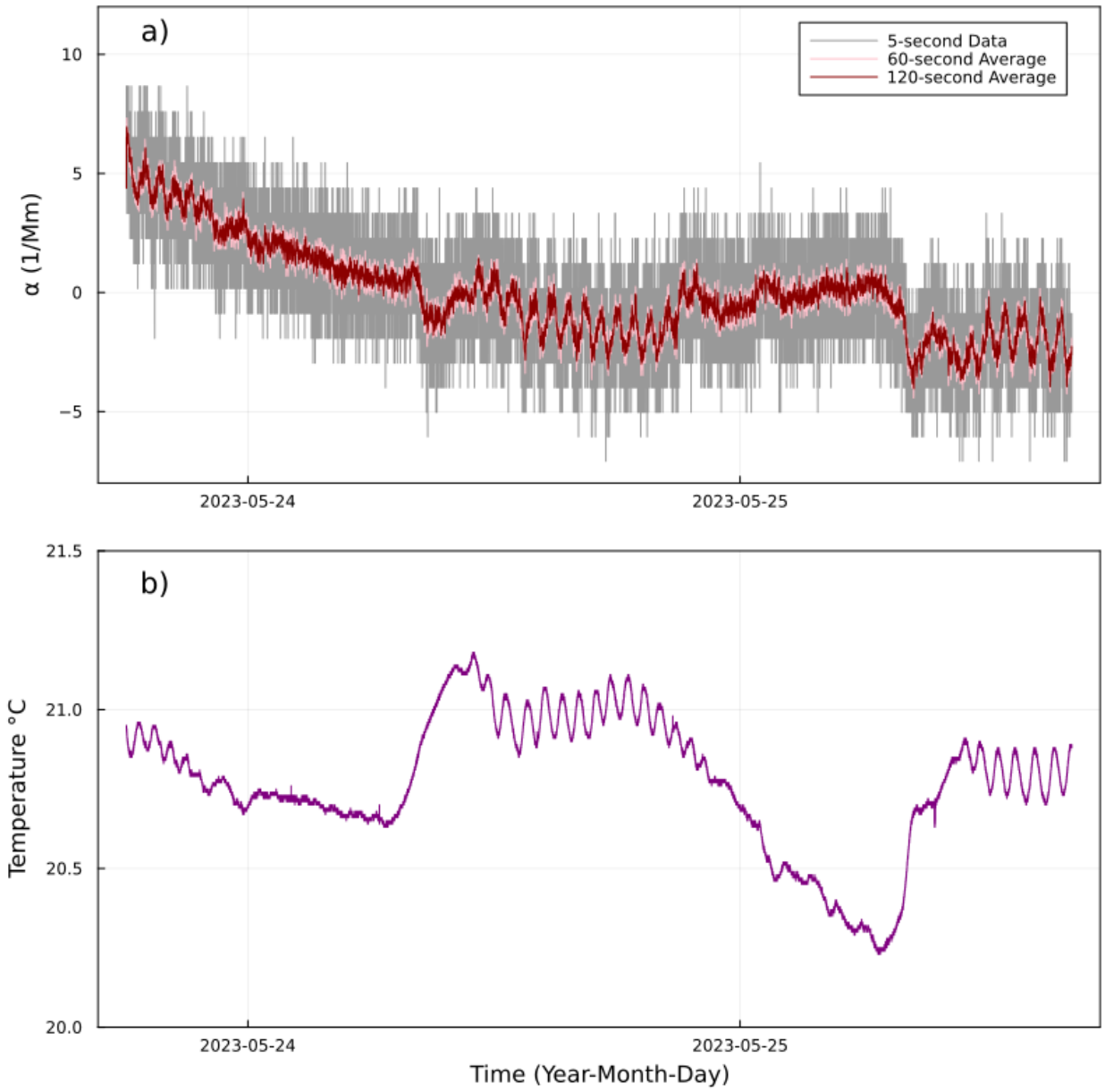

Figure 3.10. Extinction coefficient and temperature measurements of cage system (5/24/23 - 5/25/23)

Using this data to complete an Allan deviation calculation (Fig. 3.11) the results are slightly worse than the kinematic system data shown in Figure 3.7. The ultimate LOD was 0.23 Mm^{-1} at an optimal averaging time of 235 s. The ultimate LOD between the kinematic system and cage

system are the same. The difference between the kinematic system and the cage system Allan deviation calculations is the optimal averaging time, and repeatability of deviation results. The difference in optimal averaging time is 89 s, which means the cage system drifts slightly faster than the kinematic system. This could be due to the temperature fluctuations shown in Figure 3.10, but more testing needs to be done. The other difference was that even with those unusual temperature fluctuations not seen before, each time an Allan deviation analysis was run, it was consistent with the previous results. This meant that the cage system was more stable than the kinematic system and provided promising insight into its consistency with measurements.

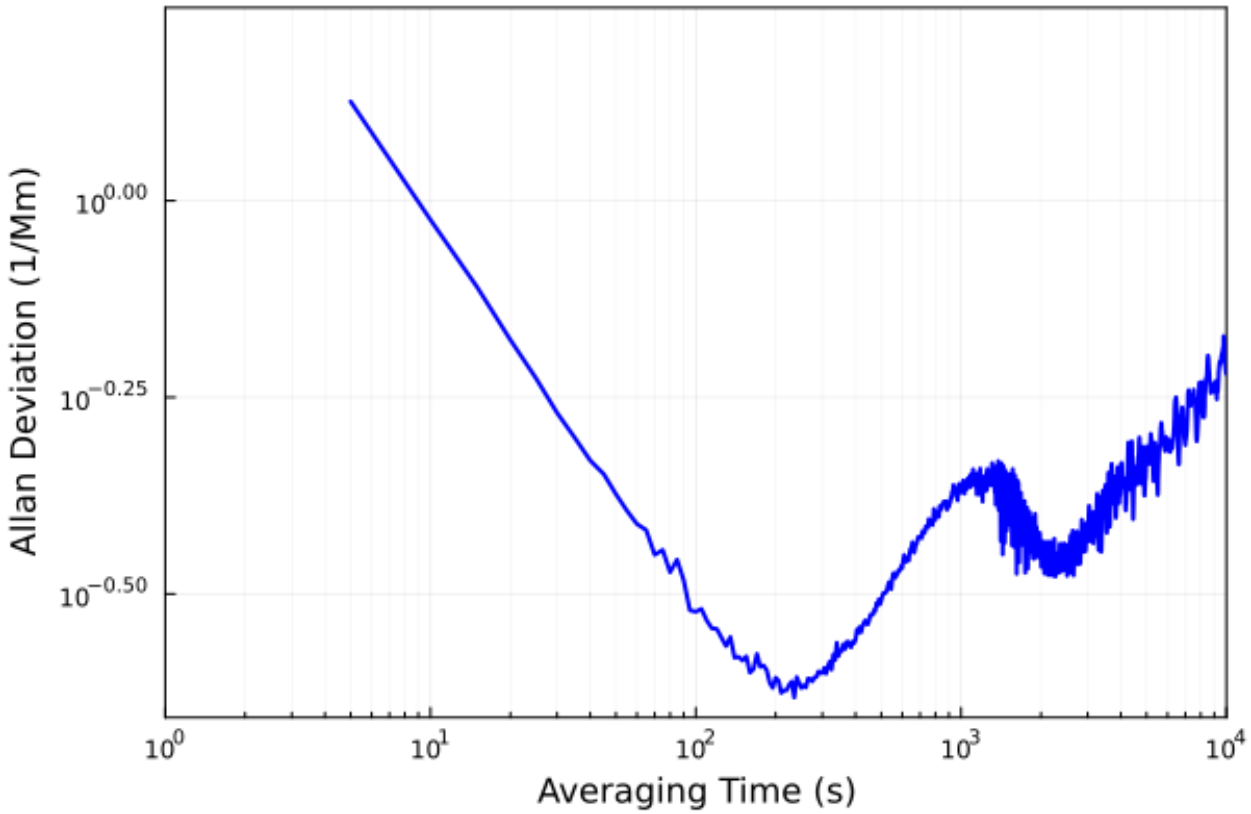

Figure 3.11. Allan Deviation of extinction coefficient using cage system data from Figure 3.10

Table 3 shows a compilation spread of cage Allan deviations results. These results include the

previously displayed measurement and three additional ones. Unlike the kinematic system, every measurement conducted for the cage system resulted in a comprehensible result. The decrease in failed results increases the likelihood of the cage system being more reliable and stable.

Date	**LOD**	**Avg. Time**
2023-04-29	0.36 Mm^{-1}	85 s
2023-05-01	0.37 Mm^{-1}	85 s
2023-05-05	0.48 Mm^{-1}	505 s
2023-05-24	0.23 Mm^{-1}	235 s
Mean	0.36 Mm^{-1}	227 s
SD	0.10 Mm^{-1}	198 s
RSD	28.4 %	87.1 %

Table 3. Cage system Allan deviation results tabulated, with the mean, standard deviation (SD), and relative standard deviation (RSD) of the ultimate LOD and optimal averaging times at the bottom.

Figure 3.12 shows the Figure 3.10 extinction coefficient data averaged the same way as Figure 3.8. Using the 2σ method used before the actual LOD was calculated to be 3.0 Mm^{-1}. A decrease in performance compared to the kinematic system, by about 88%.

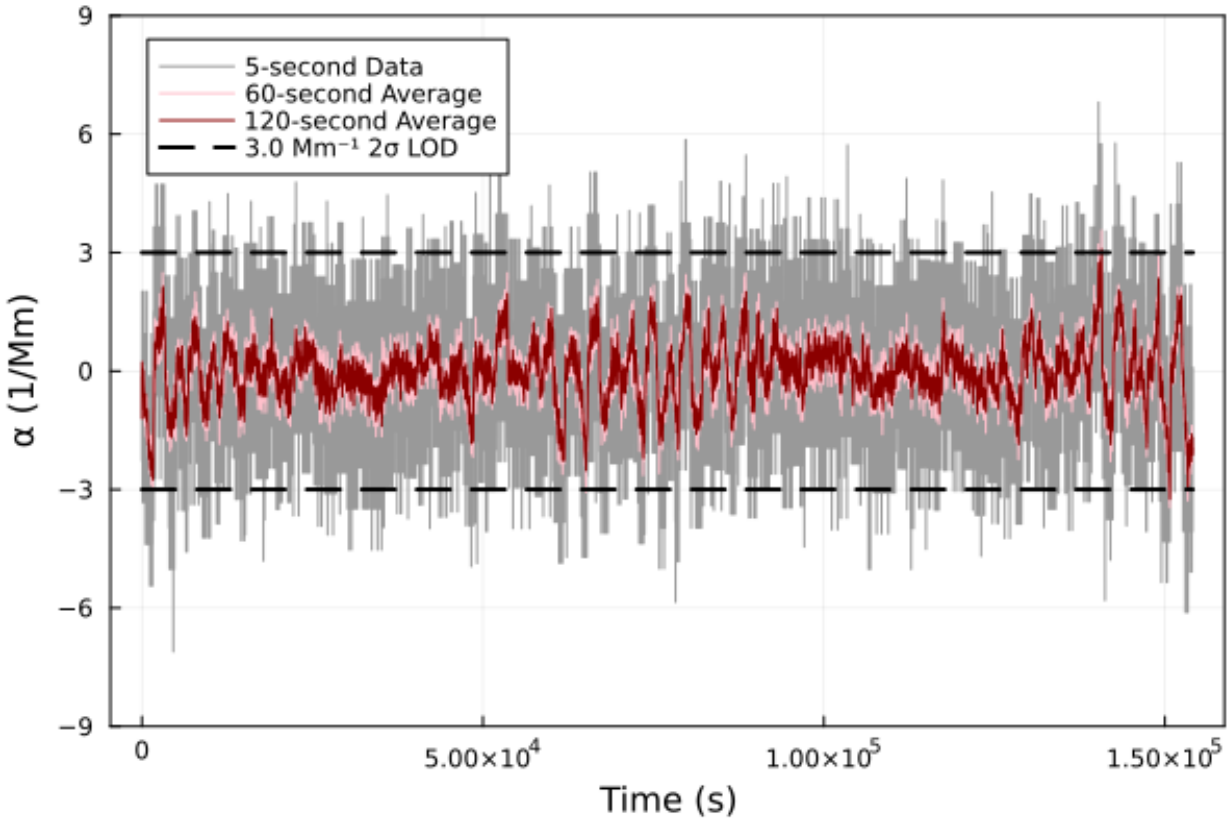

Figure 3.12. Realistic extinction coefficient using a 30 minute interval breakup from data in Figure 3.10, measured by the cage system.

Absorption Cross Section Validation

To test the accuracy and reliability of the kinematic system CRDS, the absorption cross section of different analytes was measured and compared against literature values. Absorption cross section is similar to molar absorptivity as it is a property of an analyte. Absorption cross section is the effective area that will interact with light for a single molecule. It is the probability of a single molecule absorbing light at a specific wavelength. Absorption cross section can be used for validating CRDS measurements (Eqs. 4).[25]

$$\sigma = \frac{\alpha}{N} \tag{4}$$

Where σ is the absorption cross section in cm^2/molecule at a specific wavelength, α is the extinction coefficient in cm^{-1}, and N is the number density in molecule/cm^3.

CRDS results are typically reported as the extinction coefficient, and with a known number density, the absorption cross-section can be calculated for a given analyte. Comparing the measured absorption cross section values to literature values provides insight into the accuracy of the CRDS, with a 10% variation being nominal. The two analytes used for the validation tests were O_3 and NO_2. All literature cross absorption values used were obtained from the Spectral Atlas.[27] The literature absorption cross section values at 445 nm were averaged if the dataset was high-resolution. All literature values used are at or near room temperature (298 K) and atmospheric pressure (1 atm).

Validation

Ozone was used to validate the kinematic system. Using an ozone generator, the O_3 could be trapped for the validation tests. This, however, created a situation where the concentration of the O_3 flowing out of the trap was unknown. To determine the O_3 concentration an Agilent™ Cary5000 was used to measure the absorbance at 254 nm, inline with the CRDS. Using Equation 5 the number density can be calculated using the Cary5000 data at 254 nm, which is standard for measuring O_3 concentration.[28]

$$A = \sigma b N \tag{5}$$

Where A is absorbance, σ ($1.1 \times 10^{-17}$$cm^2$/molec) is the absorption cross section for ozone at 254 nm, b is the pathlength of the absorption cell (10 cm), and N is the number density.

The O_3 number density measured using the Cary5000 represents the concentration after dilution by mirror purge. With the mirror purge, the actual number density within the CRDS is slightly lower due to a dilution with nitrogen. A dilution factor was used in the final O_3 num-

ber density calculation based on the difference in nitrogen dilution measured by the CRDS and Cary5000. Figure 3.13 represents the accurate O_3 number density and the extinction coefficient measured by the CRDS simultaneously.

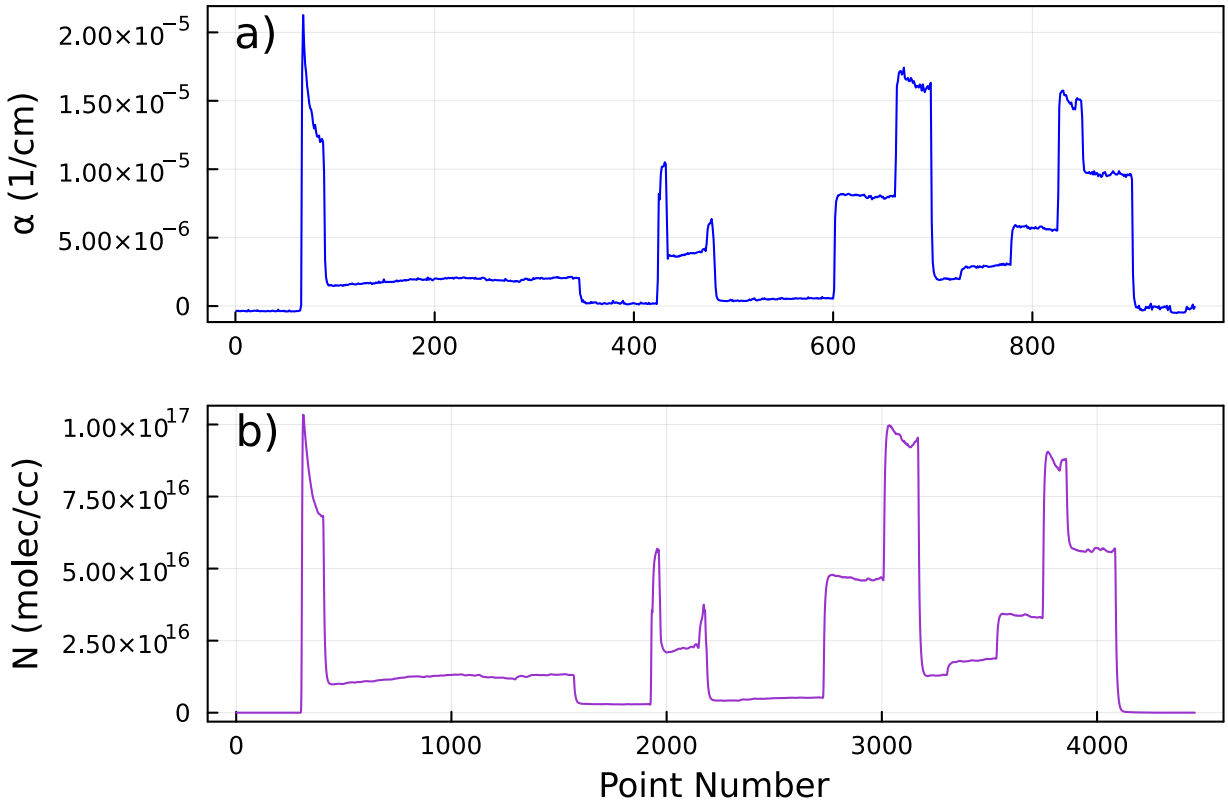

Figure 3.13. Measured extinction coefficient of O_3 using kinematic system (a), and measured O_3 number density using the Cary5000 (b), simultaneously.

Since the data, both the extinction coefficient and number density, are continuous, the data had to be broken up into sections that best correlated number density to the extinction coefficient. Six sections between the number density and extinction coefficient that aligned (Fig. 3.13) were averaged and used to calculate the O_3 absorption cross section. These sections were plateaued areas where the data was not too noisy and varied in number density enough to calculate a linear

regression properly. Figure 3.14 shows the linear regression of the measured data compared to literature values.

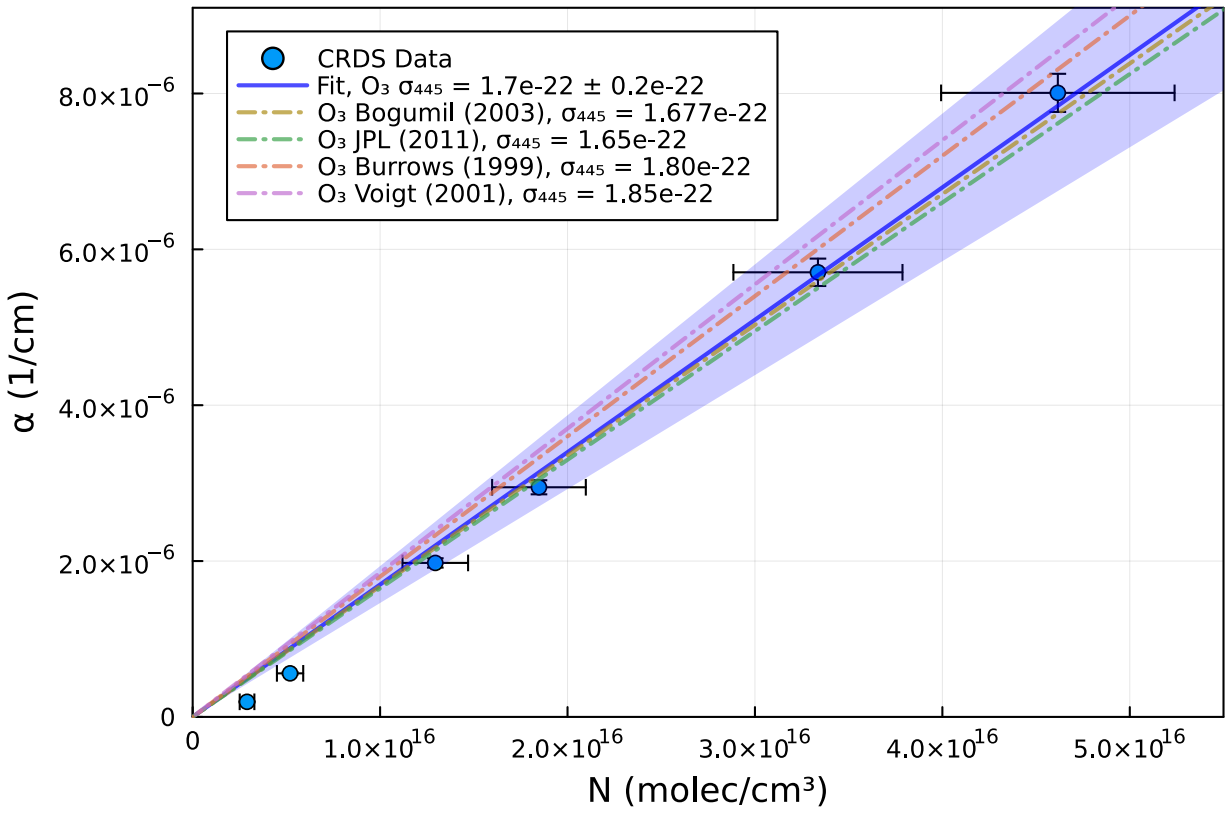

Figure 3.14. Linear regression of the data from Figure 3.13 with literature σ_{O_3-445}. The shaded blue region is the experimental uncertainty at $\pm$ 0.2 $\times$ 10^{-22} cm^2/molec. Error bars are the propagated uncertainty from the number density (x-axis) and the extinction coefficient (y-axis).

Based on the data shown in Figure 3.13, the measured σ_{O_3-445} is $1.7 \times 10^{-22} \pm 0.2 \times 10^{-22}$ cm^2/molec (Fig. 3.14). The measured σ_{O_3-445} falls within an 8% difference of the literature values. The uncertainty of σ_{O_3-445} is $\pm$14% which is larger compared to literature uncertainties ($\pm$4.8%) in the same wavelength range (410-520 nm).[29] The dominant uncertainty is caused by the number density ($\sim\pm$14%). This is due to the uncertainties of the rotameters, two were used, and each was $\pm$5% full scale. The uncertainty of the extinction coefficient is at most $\pm$3%.

The next validation used NO_2 as a standard to validate the kinematic system CRDS. Opposed to O_3, NO_2 can be readily bought from a supplier. This makes the number density easier to calculate and does not require another tandem instrument such as the Cary5000. The σ_{NO_2-445} measurements for the kinematic system did not take place at WCU and instead took place at the University of Georgia (UGA). This was a collaborative effort to compare our kinematic system CRDS to a pre-established system.

At UGA 3 different instruments including ours required NO_2 and N_2, but only 2 are comparable: WCU 445 CRDS and UGA 445 CRDS. N_2 was mixed in to dilute the NO_2 flow and regulate the final concentration. An Alicat™ mass flow controller regulated the flow rate of the NO_2 and N_2 mixture while flow regulators controlled the N_2 purge flow. Each instrument received the same NO_2 and N_2 mixture with the only variations being the purge flow dilutions.

Figure 3.15 displays the kinematic system σ_{NO_2-445} data along with literature σ_{NO_2-445} values.

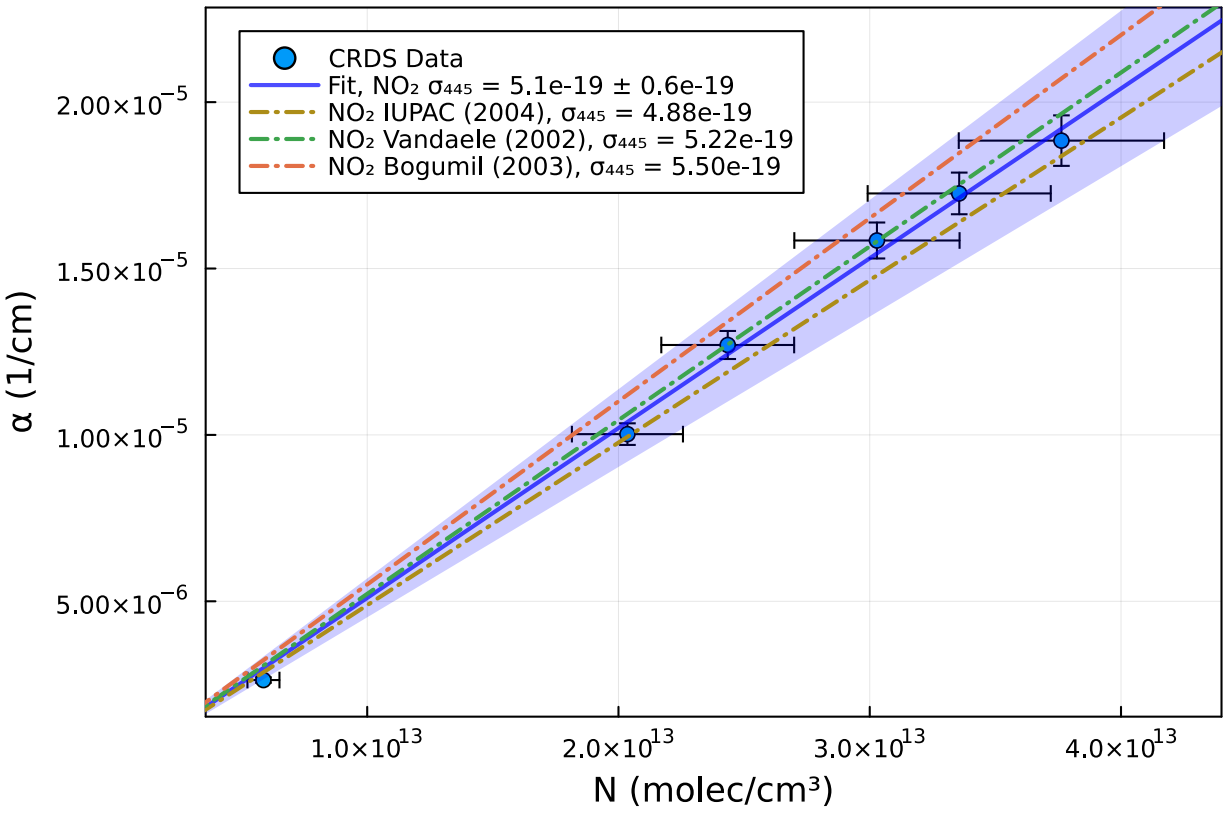

Figure 3.15. WCU CRDS σ_{NO_2-445} and literature σ_{NO_2-445}. The shaded blue region is the experimental uncertainty at $\pm$ 0.6 $\times$ 10^{-19} cm^2/molec. Error bars are the propagated uncertainty from the number density (x-axis) and the extinction coefficient (y-axis).

From Figure 3.15, the σ_{NO_2-445} ($5.1 \times 10^{-19} \pm 0.6 \times 10^{-19}$ cm^2/molec) agrees closely with literature values, with the biggest percent difference being 7%. The uncertainty of the σ_{NO_2-445} is $\pm$11% which is larger compared to previous studies ($\pm$5%) in the same wavelength range (390-460 nm).[29] The dominate uncertainty is the number density ($\sim\pm$11%). As with the ozone measurement, the rotameters have a high uncertainty associated with them, but only 1 was used this time. The uncertainty of the extinction coefficient is at most $\pm$4%.

WCU vs. UGA CRDS

The next step is to see how it performed against a high-cost CRDS. The UGA 445 CRDS was set up to measure in tandem with the kinematic system during the σ_{NO_2-445} validation. A compari-

son can be calculated and visualized using the data collected during the measurement shown in Figure 3.15. Figure 3.16 shows the UGA σ_{NO_2-445} along with the WCU CRDS σ_{NO_2-445} and a literature σ_{NO_2-445}.

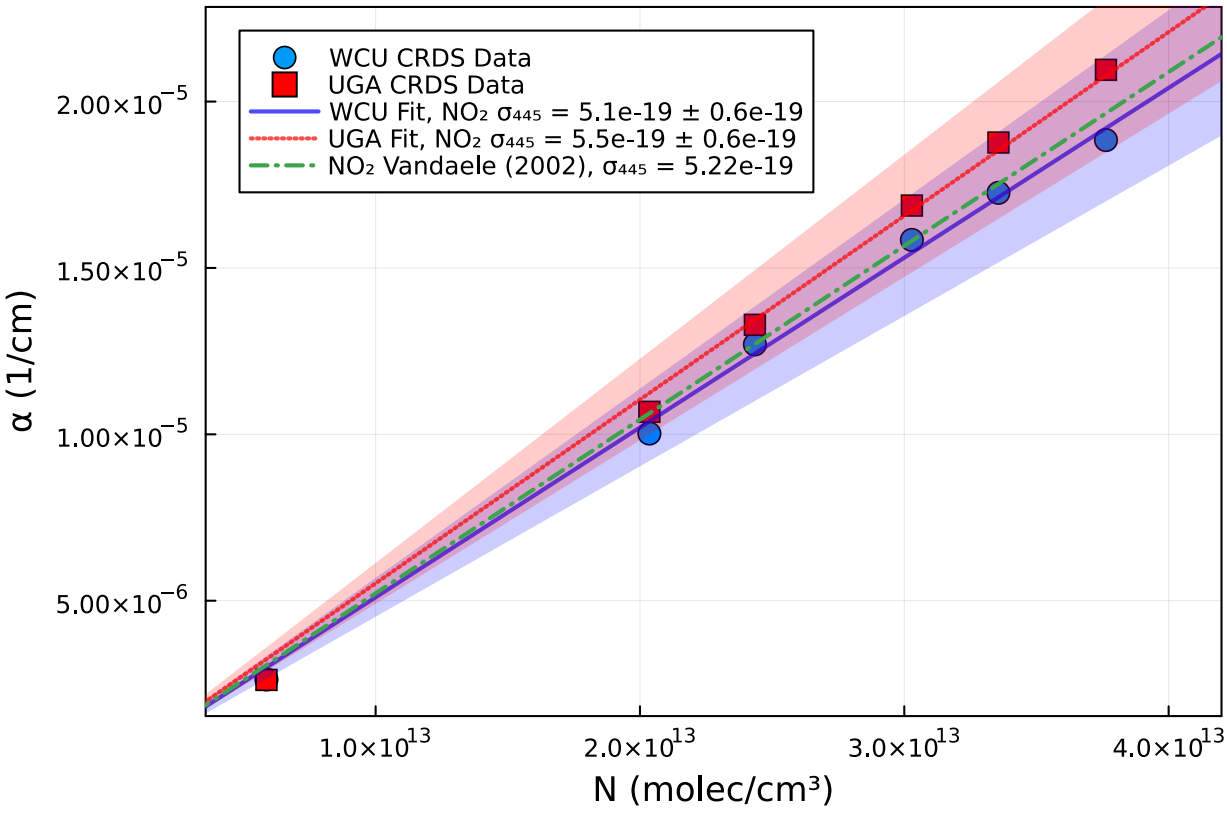

Figure 3.16. UGA CRDS σ_{NO_2-445} along with the WCU CRDS σ_{NO_2-445} and a literature σ_{NO_2-445}. The transparent blue region is the uncertainty of the WCU CRDS σ_{NO_2-445}, and the transparent red is the uncertainty of the UGA CRDS σ_{NO_2-445}.

From Figure 3.16 the UGA σ_{NO_2-445} ($5.5 \times 10^{-19} \pm 0.6 \times 10^{-19}$ cm^2/molec) agrees closely within the other displayed literature values, with the biggest percent difference being 10%. The uncertainty of the σ_{NO_2-445} is $\pm 11\%$. A similar situation to the kinematic system is the dominant uncertainty coming from the rotameter. The UGA CRDS normally does not have such a high

uncertainty rotameter. The uncertainty of the extinction coefficient is at most $\pm 2\%$.

The WCU CRDS and UGA CRDS are within the range of values reported in the literature. The uncertainty in the WCU and UGA CRDS was $\pm 11\%$. The goodness of fit for each linear regression was 0.996. The different measured σ_{NO_2-445} values could likely stem from how gas lines were set up, causing slight variations in the actual number density between instruments.

Future Directions

Measurements

Time constraints and other factors caused the cage system to not undergo the same absorption cross section validation measurements as the kinematic system. Moving forward, these measurements will be valuable for a more direct performance comparison between the two systems. The comparison between the cage system and the UGA system would also provide another comparison at a different time, giving more research data.

Cage Design

PETG was used as the printing material because of it's chemical restive properties, especially against ozone. Since the inlet and outlet ports thread into the material, there was a concern about how different analytes might react with the material. Other printing methods such as stereolithography (SLA), which is better at printing finer detail and is less susceptible to leaks, were considered but the printing material is not as chemically resistant.

A new design for the cage system could involve SLA printing and eliminate or reduce some of the complications with FDM printing, plus improve other qualities of the instrument. This design would boil down to only printing the mirror mounts and the purge ports with SLA while using metal tubing and bellows for the cavity and analyte flow ports. The analyte would come into minimal contact with the printed material because the purge gas creates a barrier. SLA prints at a finer detail than FDM, so the threads could be finer, which would improve the fit. SLA also prints in a way that has been observed to be leak resistant, which would ensure it is airtight. The metal cavity would allow chemically destructive analytes to be measured along with the analyte not sat-

urating the cavity material.

CHAPTER 4: CONCLUSION

Overall, both kinematic and cage systems performed slightly poorer than other high-cost CRDS instruments. The kinematic system had a consistent drift characteristic that seems heavily impacted by temperature. This caused long-lasting or ambient air measurements to often fail. Short-term measurements did not seem to impact the kinematic system as apparent with the absorption cross section validations. The drift was slightly mitigated with a looser spring tension on the kinematic mounts. The cage system had an improved tolerance to temperature but may still be impacted by abrupt temperature fluctuations. The cage system did mitigate the drift seen before in the kinematic system to a tolerable level and had consistent measurements and little to no failed long-term measurements.

The kinematic system's absorption cross section measurements are similar to literature values for NO_2 and O_3 at 445 nm. For the ozone measurements with the crude Cary5000 and CRDS apparatus it performed quite well. The σ_{O_3-445} was within an 8% difference of displayed literature values and had an uncertainty of $\pm 14\%$. This uncertainty is about 3 times larger than literature uncertainties at $\pm 4.8\%$ (410-520 nm), but the dominant factor in this uncertainty stems from rotameters used to control flows. The σ_{NO_2-445} measurement depicts a similar story to the σ_{O_3-445}. It performed within a 7% difference of displayed literature values and had an uncertainty of $\pm 11\%$. σ_{NO_2-445} literature values deviate by about $\pm 5\%$ (390-460 nm). The rotameter uncertainty, again, is the dominant factor for the experimental uncertainty. Changing to a rotameter with a lower uncertainty or a mass flow controller would decrease the uncertainty by about a factor of 2, putting it close to literature values. The low-cost WCU instrument performed similarly to the UGA instrument. More validations need to be conducted, especially with the cage system, but as initial results these are promising.

Comparing Allan deviation results between both system designs shows a clear difference in performance. The kinematic system had Allan deviation measurement problems that resulted

in only a few measurements being clean enough to interpret. In Fischer and Smith[23] their 662 CRDS had an ultimate LOD of <0.1 Mm^{-1} at over 1000 s while the best kinematic ultimate LOD was 0.16 Mm^{-1} at 324 s. The realistic LOD reported by Fischer and Smith[23] was 0.54 Mm^{-1} while the kinematic was 1.6 Mm^{-1}.

The cage system was more stable than the kinematic system and deviated less in its performance. The cage system had its best ultimate LOD at 0.23 Mm^{-1} with an averaging time of 235 s and a realistic (2σ) LOD of 3.0 Mm^{-1}. While the kinematic system varied more from day to day.

Both systems show promise in performing better with fine tuning. The kinematic system would need a better way to deal with the temperature drift, likely by changing the kinematic mounts to a different style or applying external pressure to the mounts to keep the springs from changing with temperature. The cage system performs comparably to the kinematic system and provides better measurement stability. Both are low-cost instruments with the cage system having the ability for faster prototyping modifications and long term cost reduction by manufacturing most of the parts even with future direction modifications.

REFERENCES

[1] Tohidi, R.; Altuwayjiri, A.; Pirhadi, M.; Sioutas, C. Quantifying ambient concentrations of primary and secondary organic aerosol in central Los Angeles using an integrated approach coupling source apportionment with regression analysis. *Atmospheric Environment* **2022**, *268*, 118807.

[2] Ghan, S. J.; Schwartz, S. E. Aerosol Properties and Processes: A Path from Field and Laboratory Measurements to Global Climate Models. *Bulletin of the American Meteorological Society* **2007**, *88*, 1059–1084.

[3] Fried, A.; Diskin, G.; Weibring, P.; Richter, D.; Walega, J. G.; Sachse, G.; Slate, T.; Rana, M.; Podolske, J. Tunable infrared laser instruments for airborne atmospheric studies. *Applied Physics B* **2008**, *92*, 409–417.

[4] Chemical and microphysical characterization of ambient aerosols with the aerodyne aerosol mass spectrometer. *Mass Spectrometry Reviews* **2007**, *26*, 185–222, https://doi.org/10.1002/mas.20115.

[5] Gagliardi, G.; Loock, H.-P. In *Cavity-Enhanced Spectroscopy and Sensing*; Gagliardi, G., Loock, H.-P., Eds.; Springer Berlin Heidelberg, 2014; Vol. 179.

[6] Maity, A.; Maithani, S.; Pradhan, M. Cavity Ring-Down Spectroscopy: Recent Technological Advancements, Techniques, and Applications. *Analytical Chemistry* **2021**, *93*, 388–416.

[7] Berden, G.; Engeln, R. *Cavity Ring-Down Spectroscopy; Techniques and Applications*; Wiley, 2009; p 322.

[8] Urban, P. L. Prototyping Instruments for the Chemical Laboratory Using Inexpensive

Electronic Modules. *Angewandte Chemie International Edition* **2018**, *57*, 11074–11077, https://doi.org/10.1002/anie.201803878.

[9] Dragone, V.; Sans, V.; Rosnes, M. H.; Kitson, P. J.; Cronin, L. 3D-printed devices for continuous-flow organic chemistry. *Beilstein Journal of Organic Chemistry* **2013**, *9*, 951–959.

[10] Lunden, M. M.; Parworth, C. L.; Barkjohn, K. K.; Holder, A. L.; Frederick, S. G.; Clements, A. L. Correction and Accuracy of PurpleAir PM 2.5 Measurements for Extreme Wildfire Smoke. **2022**,

[11] Joly, L.; Maamary, R.; Decarpenterie, T.; Cousin, J.; DumeliÃl', N.; Chauvin, N.; Legain, D.; Tzanos, D.; Durry, G. Atmospheric Measurements by Ultra-Light SpEctrometer (AMULSE) Dedicated to Vertical Profile in Situ Measurements of Carbon Dioxide (CO2) Under Weather Balloons: Instrumental Development and Field Application. *Sensors* **2016**, *16*.

[12] Stevens, R. E.; Hsiao, C. W.; Le, L.; Curro, N. J.; Monton, B. J.; Chang, B. Y.; Kung, C. Y.; Kittrell, C.; Kinsey, J. L. A partial pressure monitor and controller for stable ozone flow from a silica gel trap. *Review of Scientific Instruments* **1998**, *69*, 2504–2509.

[13] Coleman, E.; Siegrist, T.; Mixon, D. A.; Trevor, P. L.; Trevor, D. J. A versatile lowâĂŘpressure ozone source. *Journal of Vacuum Science Technology A* **1991**, *9*, 2408–2409.

[14] Bezanson, J.; Edelman, A.; Karpinski, S.; Shah, V. B. Julia: A fresh approach to numerical computing. *SIAM Review* **2017**, *59*, 65–98.

[15] van Rossum, G. *Python tutorial*; 1995.

[16] Wheeler, M. D.; Newman, S. M.; Orr-Ewing, A. J.; Ashfold, M. N. Cavity ring-down spectroscopy. *Journal of the Chemical Society, Faraday Transactions* **1998**, *94*, 337–351.

[17] Mogensen, P. LsqFit. https://github.com/JuliaNLSolvers/LsqFit.jl, 2022; Version 0.13.0.

[18] Salceanu, A. Genie Framework. https://genieframework.com, 2023; Version 1.19.

[19] Riley, W.; Howe, D. *Handbook of Frequency Stability Analysis*; 2008.

[20] Land, D. V.; Levick, A. P.; Hand, J. W. The use of the Allan deviation for the measurement of the noise and drift performance of microwave radiometers. *Measurement Science and Technology* **2007**, *18*, 1917.

[21] Kluge, J. AllanDeviations. https://github.com/JulienKluge/AllanDeviations.jl, 2022; Version 0.3.

[22] Riley, W.; Time, P. L. U.; Division, F. *Handbook of Frequency Stability Analysis*; NIST special publication; U.S. Department of Commerce, National Institute of Standards and Technology, 2008.

[23] Fischer, D. A.; Smith, G. D. A portable, four-wavelength, single-cell photoacoustic spectrometer for ambient aerosol absorption. *Aerosol Science and Technology* **2018**, *52*, 393–406, doi: 10.1080/02786826.2017.1413231.

[24] Nakayama, T.; Suzuki, H.; Kagamitani, S.; Ikeda, Y.; Uchiyama, A.; Matsumi, Y. Characterization of a Three Wavelength Photoacoustic Soot Spectrometer (PASS-3) and a Photoacoustic Extinctiometer (PAX). *Journal of the Meteorological Society of Japan. Ser. II* **2015**, *93*, 285–308.

[25] Fuchs, H.; Dubé, W. P.; Lerner, B. M.; Wagner, N. L.; Williams, E. J.; Brown, S. S. A sensitive and versatile detector for atmospheric NO2 and NOx based on blue diode laser cavity ring-down spectroscopy. *Environmental science & technology* **2009**, *43 20*, 7831–6.

[26] Wild, R. J.; Edwards, P. M.; Dubé, W. P.; Baumann, K.; Edgerton, E. S.; Quinn, P. K.; Roberts, J. M.; Rollins, A. W.; Veres, P. R.; Warneke, C.; Williams, E. J.; Yuan, B.;

Brown, S. S. A measurement of total reactive nitrogen, NOy, together with NO2, NO, and O3 via cavity ring-down spectroscopy. *Environmental Science and Technology* **2014**, *48*, 9609–9615.

[27] Keller-Rudek, H.; Moortgat, G. K.; Sander, R.; Sörensen, R. The MPI-Mainz UV/VIS Spectral Atlas of Gaseous Molecules of Atmospheric Interest. *Earth System Science Data* **2013**, *5*, 365–373.

[28] Williams, E. J.; Fehsenfeld, F. C.; Jobson, B. T.; Kuster, W. C.; Goldan, P. D.; Stutz, J.; McClenny, W. A. Comparison of ultraviolet absorbance, chemiluminescence, and DOAS instruments for ambient ozone monitoring. *Environmental Science and Technology* **2006**, *40*, 5755–5762.

[29] Orphal, J. A critical review of the absorption cross-sections of O 3 and NO 2 in the ultraviolet and visible. *Journal of Photochemistry and Photobiology A: Chemistry* **2003**, *157*, 185–209.